Rheology and breakdown energy of a shear zone undergoing flash heating in earthquake-like discrete element models

Alfredo Taboada, Mathieu Renouf

Geophysical Journal International

Geophys. J. Int. (2023) **233,** 1492–1514
Advance Access publication 2023 January 05
GJI Rock and Mineral Physics, Rheology

https://doi.org/10.1093/gji/ggad004

Rheology and breakdown energy of a shear zone undergoing flash heating in earthquake-like discrete element models

A. Taboada[1] and M. Renouf[2]

[1]*Géosciences Montpellier, Université de Montpellier, CNRS, Montpellier, France. E-mail: alfredo.taboada@umontpellier.fr*
[2]*LMGC, UMR 5508, CNRS, Université de Montpellier, Montpellier, France*

Accepted 2023 January 4. Received 2022 October 27; in original form 2021 November 17

SUMMARY

We study the initiation and growth of a dry granular shear zone subjected to seismic shearing and flash heating from the perspective of a discrete element method. For this purpose, we created a semi-periodic numerical shear test similar to a rotary shear machine in which a 2 mm $\times$1.5 mm sample composed of micrometric cohesive disks is sheared in between two rigid walls. The strength of cohesive bonds is defined according to an elasto-brittle contact law calibrated to simulate peak and residual strength envelopes derived from rock mechanics tests. The sample is traversed by a pre-existing fracture and subjected to a vertical confining pressure (e.g. 112.5 MPa) and a velocity step function (e.g. 1 m s^{-1}) applied on the top and bottom walls, respectively. Slip along the fracture induces the growth of a shear zone, which thickens by progressive abrasion of damaged material from cohesive blocks. We carried out two parametric studies to determine the rheology and physical properties of the shear zone for slip velocities and confining pressures characteristic of shallow earthquakes and several flash-heating temperatures. According to parametric studies, the mechanical behavior of the shear zone exhibits three distinct phases. The initial phase of rupture initiation is characterized by the propagation of a shear instability generated by the velocity step (phase 1). During this phase, friction and dilatancy curves are approximated by asymmetric peak functions whose amplitude and geometry are controlled primarily by confining pressure. In the intermediate phase of shear-zone growth, the sample displays an initial transient stage that asymptotically approaches steady state at submelting temperatures (phase 2). According to the inertial number, seismic shearing occurs under quasi-static conditions despite high shear rates. Thus, friction and dilatancy observed in all simulations are roughly constant regardless of slip velocity, confining pressure, and gouge zone thickness. In the final phase of shear weakening, the model evolves toward a new steady state at flash-heating temperatures (phase 3). Average friction and dilatancy are represented by sigmoidal decreasing curves that approach steady-state values lower than for phase 2. Predictably, the thermally weakened friction in steady state ($\mu_{ss} \sim 0.1$) is close to the strength of frictionless granular samples sheared in quasi-static conditions. We calculate breakdown energies for the gouge and damage zones and the fracture energy at intermediate and high confining pressures. We show that breakdown energy fundamentally differs from fracture energy commonly used in seismology. The breakdown energy of the damage zones shows long-period damped oscillations weakly correlated with shear-stress fluctuations around average decaying values. Our results suggest that dilatancy is the primary energy sink within the damage zones at steady-state values. The breakdown energy components of the gouge zone follow a similar decaying trend as the average fracture energy but over a longer critical distance. Decohesion and dilatancy are the major energy sinks linked to gouge formation at intermediate pressures. In contrast, dilatancy and debonding frictional energies predominate at high confining pressures. Breakdown energy is equivalent to a fraction of fracture energy that nearly triples when doubling the confining pressure.

Key words: Microstructure; Numerical model ling; Earthquake dynamics; Rheology and friction of fault zones; Dynamics and mechanics of faulting; Fractures, faults, and high strain deformation zones.

1 INTRODUCTION

Seismic faulting is associated with slip across a gouge layer of millimetric or sub-millimetric thickness composed of ultra fine-grained material, which is sheared under extreme conditions of confining pressure, temperature, and shear rate (Chester & Goldsby 2003; Boullier *et al.* 2009; Bradbury *et al.* 2011; Smith *et al.* 2011; Verberne *et al.* 2014; Togo *et al.* 2016; Nielsen 2017; Smeraglia *et al.* 2017). The complex rheology of fault gouge is one of the major factors controlling the velocity-weakening friction responsible for potentially unstable, fast seismic slip, in which shear strength decreases with increasing slip rate (Scholz 1998). Two major mechanisms have been extensively discussed to explain the dynamic weakening of fault zones subjected to rapid shearing at high confining pressures (Rice 2017, and references therein). The first involves flash-heating and weakening of highly stressed asperity contacts between sliding surfaces of cohesive rock. The second involves thermal pressurization of the pore fluid that results from temperature rise and overpressure of native ground fluids by frictional heat dissipation (Lachenbruch & Sass 1980; Andrews 2005; Sulem *et al.* 2005; Faulkner *et al.* 2018; Acosta *et al.* 2018; Chen *et al.* 2019). These mechanisms are interconnected with other dynamic-weakening mechanisms identified through experimental studies on fault gouge sheared at the high slip rates and large sliding displacements characteristic of earthquakes (Di Toro *et al.* 2011). The most significant are melt lubrication (Di Toro *et al.* 2006), powder lubrication (Reches & Lockner 2010; Wang *et al.* 2017), and fault lubrication by different physicochemical processes such as gelification (Goldsby & Tullis 2002; Kirkpatrick *et al.* 2013), decarbonation (Sulem & Famin 2009; Collettini *et al.* 2013), and dehydration reactions (Han *et al.* 2014).

The conceptual micromechanical model for frictional weakening by flash heating supposes that the shear surface consists of a large set of microscopic rock-on-rock asperity contacts subjected to very high stresses (e.g. Rice 2006; Aharonov & Scholz 2018; Nielsen *et al.* 2021). The frictional strength at asperity contacts is defined by the ratio between shear strength and normal stress and varies between 0.6 and 0.8 at low slip rates and temperatures, following Byerlee's friction law. In quasi-static conditions, the contact indentation strength σ_c determines the normal stress at asperity contacts. In addition, the shear strength τ_c is of the order of $0.1G$ where G is the elastic shear rigidity (Dieterich & Kilgore 1996). Flash heating involves dynamic slip along the shear surface, which induces a local rise in temperature at asperity contacts that are heated too rapidly for conduction to dissipate the thermal energy released by mechanical work. Localized heating causes thermal softening at asperity contacts inducing a sharp drop in shear strength, while the indentation strength is not expected to change (Beeler *et al.* 2008; Aharonov & Scholz 2018). Thus, the frictional strength drops dramatically once the slip rate exceeds a critical velocity V_w generally around 0.1–1 cm s^{-1} (earthquake slip rates are typically around 1 m s^{-1}).

Experimental studies suggest that thermal pressurization of the fault fluid is the dominant mechanism of dynamic weakening at mid-crustal depths (∼2–5 km) because flash heating is inhibited by water's liquid-supercritical phase transition (∼373 °C at 25 MPa), which buffers frictional heat (Acosta *et al.* 2018). However, the efficiency of the heat buffer is strongly reduced when fluid pressures reach 70 MPa (∼7 km depth). Further studies have shown that the rheology of saturated fault gouge subjected to seismic shearing is more complex and depends on host-rock composition (Violay *et al.* 2014): in silicate bearing rocks (e.g. microgabbros), the initial weakening mechanism (flash heating of the asperities) is delayed in the presence of water; conversely, in calcite marble, the weakening mechanism (brittle failure of the asperities) is favored. Elementary physical models of flash heating for large populations of asperity contacts are in reasonable agreement with experimental data for many silicate rocks (Rempel & Weaver 2008; Beeler *et al.* 2008). Some authors suggest that fast-moving dislocations observed during dynamic shear are a possible micro-physical mechanism responsible for the intense grain size reduction and the high-temperature rise associated with dynamic slip in natural and experimental faults (Spagnuolo *et al.* 2016).

Seismic shear zones are complex systems in which strain patterns and macroscopic properties such as friction and dilatancy emerge from the collective behavior of individual grains and asperities that interact through contact forces (Rognon *et al.* 2006; Ben-David & Fineberg 2011). In addition, the external loading configuration also controls friction, which is not a constant material property (Ben-David & Fineberg 2011), and the process of dynamic organization that interrelates particle-scale properties with properties at macroscopic scale is still enigmatic (Vakis *et al.* 2018, and references therein). On the one hand, the vast majority of numerical and theoretical approaches oversimplify the behavior of the shear zone by ignoring the granular nature of fault gouge and supposing that it behaves as a continuum or a plane with a negligible thickness (Rempel & Rice 2006; Rice *et al.* 2014; Brantut & Viesca 2017; Faulkner *et al.* 2018). These theoretical approaches often introduce phenomenological laws such as the classic rate and state friction that approximate macroscopic shear strength as a function of state variables (Tinti *et al.* 2016). On the other hand, experimental studies cannot measure the evolution of local physical parameters such as contact forces and temperatures or particle kinematics. They can only provide information on macroscopic parameters or describe the final state of the sheared samples. Thus, more realistic approaches are sought to investigate the micromechanical origin of dynamic weakening based on a granular description of fault gouge. Discrete element models allow for the integration of the main processes at the particle scale, namely, the mechanical interactions between grains (cohesive bonds and frictional contact forces), energy dissipation by debonding, friction, dilatancy and heat transfer.

There is deep uncertainty regarding the energy consumed in breaking down the rocks during coseismic slip in shallow earthquakes (Johnson *et al.* 2021, and references therein). Furthermore, breakdown energy dissipated in generating the gouge and surrounding damage zones is difficult to quantify as it involves a variety of inelastic physical mechanisms such as shear and tensile microcracking and dynamic fragmentation (Nguyen & Einav 2009; Vora & Morgan 2019). These mechanisms are coupled with frictional heat dissipation and thermal softening of the gouge, introducing greater complexity to the system (Rice 2006; Beeler 2006; Goldsby & Tullis 2011; Brantut & Viesca 2017). Accordingly, due to the lack of accurate knowledge on these processes, breakdown energy is often identified with fracture energy calculated in theoretical, experimental, and geological studies and from earthquake kinematic models (e.g. Niemeijer *et al.* 2012; Togo & Shimamoto 2012; Passelègue *et al.* 2016a).

The main objective of this work is to study the initiation and growth of a dry granular shear zone subjected to seismic shearing and flash heating using a discrete element method (Renouf *et al.* 2004; Taboada *et al.* 2005). To do so, we generated a semi-periodic numerical sample composed of micrometric cohesive disks traversed by a pre-existing fracture. The sample is subjected to a velocity step function imposed at the base of the model (i.e. the bottom wall), inducing the growth of a shear zone triggered by

slip along the fracture, which thickens by progressive abrasion and incorporation of damaged material from the cohesive blocks. We carried out several parametric studies to determine the rheology and physical properties of the shear zone for characteristic values of the state variables, namely the slip velocity, the confining pressure and the flash-heating temperature.

We show that the evolution of rheological and physical parameters, such as friction, dilatancy, damage, and temperature throughout shear-zone growth, leads to the emergence of successive transient stages and steady states at submelting and flash-heating temperatures. Additionally, we analyze the energy budget of the shear zone by calculating the fracture energy and the breakdown energies for the gouge and damage zones at intermediate and high confining pressures. These fundamental problems that we revisit from the perspective of granular materials are complementary to those addressed in the few existing studies on this topic using discrete element methods—for example, the simulation of melting in a gouge zone with a constant thickness (Mollon *et al.* 2021). This approach enables us to gain insight into the complex process of self-organization inherent to the growth of seismic shear zones.

2 NUMERICAL AND PHYSICAL FRAMEWORK

2.1 Contact dynamics overview

Discrete element methods (DEM) are ideally suited to represent the granular feature of the seismic shear zone at the local scale. DEM models dedicated to the evolution of granular media can be based either on explicit or implicit methods (Radjai & Dubois 2011). The main drawback of explicit models is to reduce non-local momentum transfers implied in multiple contacts to a succession of binary contacts. Moreover, numerical instabilities are corrected either by introducing some artificial viscosity or by reducing the time step size.

The model presented in this work is based on the contact dynamics (CD) method, which is suitable for simulating the mechanical behavior of large assemblies of rigid particles that interact through contact forces (Moreau 1988; Taboada *et al.* 2005; Radjai & Dubois 2011). It provides a non-smooth formulation of the body's impenetrability condition and the dry Coulomb friction law. A θ-method is used for time discretization, and a classical non-linear Gauss–Seidel algorithm is used to solve the system (Jean 1999). The approach benefits from a parallel version to ensure reasonable CPU times (Renouf *et al.* 2004). Nevertheless, the model is defined in 2D using disks (not polygons) to limit the computation time that can be excessively long (more than one month for some simulations). Even so, disk models are insightful for analyzing shear zone evolution at different scales (e.g. Makedonska *et al.* 2011). The method outlines are detailed in Appendix A, whereas the contact law used to simulate gouge formation is described in Section 2.2.

2.2 Strength model at contact scale

Applying DEM methods to tribology problems involving natural materials such as rocks and soils requires introducing cohesive bonds in the contact law that controls the interactions between particles (Estrada & Taboada 2013; Champagne *et al.* 2014). Cohesive bonds are simulated by implementing an elasto-brittle model suitable for monotonic or cyclic stress regimes both in extension and compression. The model involves four mechanical parameters: The normal and tangential stiffnesses (C_n and C_t), the decohesion energy per unit length (w_c), and the sliding friction coefficient between particles μ_s. For purposes of the present work, the stiffnesses are considered to be equal ($C_\mathrm{n} = C_\mathrm{t} = 10^6$ MPa), the decohesion energy is $w_\mathrm{c} = 0.08$ J m^{-1}, and the local sliding friction is $\mu_\mathrm{s} = 0.5$. In order to define the strength model at contact scale, the contact stresses in 2D are calculated as the ratio of the contact force to the equivalent radius of the disks in contact $R_\mathrm{e} = R_i R_j/(R_i + R_j)$ (i.e. stresses are given in N m^{-1}).

The shear strength of a cohesive bond is defined using a local Mohr–Coulomb failure envelope (i.e. involving friction and cohesion), in which cohesion is a function of the relative tangential displacement u_t between particles in contact (Figs 1a and b). This micromechanical model is well adapted to the simulation of contact interactions between particles larger than 1 μm, i.e. at scales involving many atoms or molecules (Vakis *et al.* 2018)—note that the average particle size in our model is 10 μm. In contrast, we have neglected van der Waals and adhesive forces, which are dominant in nanometric scale processes such as the molecular interactions between two macroscopic solids in the presence of nanoscale roughness (e.g. Kudryavtsev *et al.* 2009).

The calculation of debonding energies requires decomposing the contact shear strength into a cohesive and frictional component: $T_\mathrm{c} = T_\mathrm{c}^\mathrm{C} + T_\mathrm{c}^\mu$ (Fig. 1b). For small displacements, the cohesive shear component T_c^C is defined by a linear elastic behavior law whose slope is specified by the tangential stiffness C_t. Its maximum value is given by $\tau_\mathrm{c} R_\mathrm{e}$ at $u_t = \delta_\mathrm{c}$, where $\tau_\mathrm{c} = 0.4$ MPa m^{-1} is the cohesive contact strength per unit length and $\delta_\mathrm{c} = 0.4\,\mu$m is the decohesion distance (equivalent to ∼5 per cent of the average particle size) (blue polyline, Fig. 1a). Note that the elastic force component is mobilized once the shear force T_c reaches the frictional threshold $T_\mathrm{c}^\mu = \mu_\mathrm{s} N_\mathrm{c}$, where N_c is the normal contact stress. In other words, the shear displacement between two particles in contact initiates once the shear force surpasses the frictional threshold. The brittle behavior implies that the cohesive shear component T_c^C drops to zero for displacements larger than the critical distance δ_c (i.e. the cohesive bond breaks) while the frictional force component remains active.

The decohesion energy per unit length in shear mode is equivalent to the area below the stress–displacement elastic law $w_\mathrm{c} = \tau_\mathrm{c}\delta_\mathrm{c}/2 = 0.08$ J m^{-1} (i.e. the shaded area in light blue). Analogously, the decohesion energy linked to a specific bond is defined as $w_\mathrm{c}^\mathrm{C} = w_\mathrm{c} R_\mathrm{e}$. These energy parameters at the contact scale are used to calculate the decohesion energy of particles in the gouge zone as a function of slip displacement (Section 3.2).

The extensional strength of bonded contacts evolves as a function of the gap between particles in contact (u_n), showing a sequence of two characteristic behavior laws (*cf.* green polyline, Fig. 1a). Firstly, the bond does not contract under compressional stresses, in agreement with particle impenetrability. This behavior is illustrated by the green dashed vertical segment (normal contact stress $\sigma > 0$ is compressive). Secondly, as particles in contact move apart from each other, the contact strength enters a linear elastic domain with slope $-C_\mathrm{n}$ in which the normal stress is extensional ($u_\mathrm{n} \in]0, \delta_\mathrm{c}]$, $-\sigma_\mathrm{c} \leq \sigma < 0$, where $\sigma_\mathrm{c} = 0.4$ MPa m^{-1} is the extensional contact strength per unit length). The bond breaks when the gap exceeds the critical distance δ_c, as sketched by the green horizontal line. The model supposes that the stress–strain behavior laws for the extensional stress and the cohesive shear component are equal (i.e. the green and blue polylines are symmetric for positive displacements). In particular, the magnitude of the extensional strength σ_c is

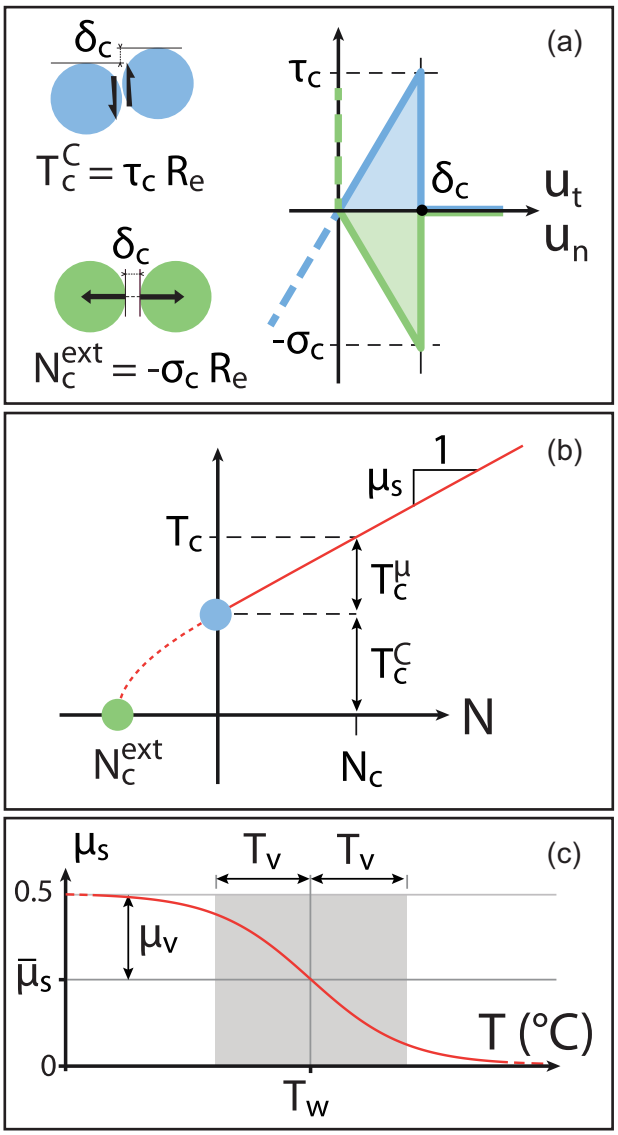

Figure 1. (a) Contact laws defining the cohesive shear stress component and the extensional stress of a cohesive bond between two particles (blue and green polylines), as a function of the relative tangential and normal displacements (u_t and u_n), respectively. Black arrows represent contact forces. (b) Mohr–Coulomb failure envelope at contact scale defining the strength of a cohesive bond. The contact shear strength is decomposed into a cohesive and a frictional component: $T_c = T_c^C + T_c^\mu$. Blue and green circles indicate the cohesive and extensional strengths of the bond. (c) Hyperbolic tangent function representing the strong decrease in contact friction with temperature, close to the flash heating threshold T_w. $\bar{\mu}_s = 0.25$ is the average friction at temperature T_w, $\mu_v = 0.25$ is the magnitude of its variation, T_v is the half-length of the temperature interval over which ~3/4 of the transition occurs. See explanations in the text.

equal to the cohesive strength τ_c defined previously. This simplifying assumption presumably leads to overestimating the extensional strength observed in uniaxial tests for intact rock samples relative to the rock cohesion (Hoek & Martin 2014). However, this difference has little effect on the stress–strain behavior of granular samples at the intermediate to high confining pressures considered in this study. Note that the decohesion energy per unit length in traction mode (i.e. the shaded area in light green) is equal to its counterpart in shear mode (i.e. the shaded area in light blue).

The sliding friction coefficient of particles remains constant ($\mu_s = 0.5$) both in the cohesive medium and in the gouge for temperatures below the flash-heating threshold. This hypothesis is realistic since contact friction is an intrinsic property that quantifies particle surface roughness (Brodsky *et al.* 2016). The variation of the friction coefficient with temperature is defined by a hyperbolic tangent function modulated by a scaling factor that controls the minimum (negative) slope of the curve (*cf.* Fig. 1c):

$$\mu_s = \bar{\mu}_s - \mu_v \tanh[(T - T_w)/T_v], \tag{1}$$

where $\bar{\mu}_s = 0.25$, $\mu_v = 0.25$, $T_v = 10\ ^\circ$C and T_w is the flash-heating temperature at microscale asperity contacts. Thus, to simulate flash heating, we have considered that the decrease in the friction coefficient occurs primarily in a small temperature interval (i.e. 20 °C) around the flash-heating threshold T_w. We assume that the sliding friction coefficient rapidly tends to zero once the temperature surpasses $T_w + T_v$ (i.e. particle contact is frictionless). This criterion is consistent with the abrupt fall in friction that is generally supposed in flash-heating models involving asperity contacts (Rice 2006). As shown in the simulations, the macroscopic friction coefficient above flash-heating temperatures tends to 0.1. Note that macroscopic friction is intrinsically different from contact friction at the particle scale (Taboada *et al.* 2006).

2.3 Heat generation and transfer

Heat transfer in granular materials involves different phenomena, such as conduction through particles and their contact spots, conduction and convection through the interstitial medium (gas or liquid), thermal radiation, and convection by shear dispersion (i.e. in dense granular flows) (Rognon & Einav 2010; Christov & Stone 2014). The relative contribution of each of these mechanisms can be calculated using dimensionless numbers defined as a function of the physical and geometrical properties of the granular medium and the prevailing mechanical conditions (e.g. the stress and strain regimes).

One of the most influential parameters for granular materials is the Peclet number (Pe), which characterizes the relative rates of convective and conductive heat transport within the particles in the absence of heat transfer to the ambient fluid. This parameter is commonly used for the study of dry granular media subjected to shear deformation. The average value of the Peclet number in our numerical shear tests is given by the following equation (Forgber & Radl 2018):

$$\mathrm{Pe} = \frac{\bar{d}\,\rho\,c}{4k}\dot{\gamma} \sim 0.15 < 1, \tag{2}$$

where $\bar{d} = 10^{-5}$ is the average particle diameter, $\rho = 2\,400$ kg m^{-3} is the density of particles, $c = 7\,800$ kg^{-1} K^{-1} is the heat capacity, $k = 3$ W m^{-1} K^{-1} is the thermal conductivity, and $\dot{\gamma} = 10^4$ s^{-1} is the average shear rate (the thermal conductivity and heat capacity are average values for quartz) (Cermak & Rybach 1982; Waples & Waples 2004). The average shear rate is calculated as the ratio of the average slip velocity (1 m/s) to the average thickness of the shear zone in steady state (0.1 mm). A low Peclet number may indicate that conductive heat transport is significantly greater than convective transport by heat dispersion. In such situations, we can neglect convective transport. Nevertheless, it is worth noting that shear dispersion is inherently integrated into discrete element methods since it is linked to the relative movement between neighboring particles.

To evaluate the contribution of radiation, we define an adimensional number (termed Π_2) relating the typical radiative heat flux to the characteristic thermal transport rate by conduction in a granular material, as follows (modified from Forgber & Radl 2018):

$$\Pi_2 = \frac{k_B \epsilon T_{ref}^4}{k \partial T/\partial y}, \tag{3}$$

where $k_B \approx 1.381 \times 10^{-23}$ J m^{-1} is the Boltzmann constant, $\epsilon = 0.93$ is the surface emissivity of quartz, T_{ref} is the reference temperature, and $\partial T/\partial y$ is the rate of temperature change perpendicularly to the shear zone. The maximum value for Π_2 is in the interval [5×10^{-3}, 5×10^{-2}] for reference temperatures between 500 and 1000 °C, considering a minimum rate of temperature change $\partial T/\partial y = 10^6$ K m^{-1}.This last value corresponds to a temperature difference of 10 °C between two neighboring particles. Note that much higher temperature gradients are frequently observed in our shear zone simulations (*cf.* Section 3.1). Thus, radiative heat flux is very low compared with thermal transport by heat conduction, and it can be neglected in our case studies.

Heat transfer by conduction is introduced in the numerical simulation using the thermal particle dynamics (TPD) method, which supposes that temperature within each particle does not vary significantly (Vargas & McCarthy 2001). This assumption implies that the resistance to heat transfer inside a particle is significantly smaller than the thermal resistance between particles. The Biot number, which represents the ratio of the thermal resistance at the contacts to the thermal resistance inside the particle, enables verifying the validity of the previous assumption. This number can be expressed by the following equation for dry granular materials:

$$B_i = \frac{Hr}{kA} = \frac{2a}{\pi r}, \tag{4}$$

where r is the particle's radius, a is the radius of the contact spots, and H is the contact thermal conductance that depends on the contact area and the thermal conductivity of the particles involved. The radius of contact spots is supposed to be less than a few percent of the particle radius despite the high confining pressure applied on the granular sample. Thus, the Biot number is low, and the particle temperature can be considered as uniform in a first-order approximation.

The evolution of the temperature of a single particle is determined by calculating the thermal power due to conduction with neighboring particles and the mechanical power due to energy dissipation. More precisely, we consider that the variation of local kinetic energy due to an inelastic collision or a sliding frictional contact is transformed into heat and splits between contacting particles (see Renouf & Berthier 2011, and Appendix B for details on the formulation and boundary conditions of the thermal model). It should be recalled that the contact law assumes that contact friction falls to zero when the temperature surpasses the flash-heating threshold T_w. Therefore, the maximum temperature in the granular systems is, at most, slightly higher than T_w since frictionless contacts dissipate only a limited amount of energy through particle collisions (*cf.* Section 3.1).

Although the weakening temperature T_w is generally associated with the melting temperature or thermal decomposition temperature of rock minerals, the precise mechanisms for strength loss are not clear and do not necessarily correspond to conventional melting (Brantut & Platt 2017). For example, minerals like quartz can be amorphized and form a gel-like layer that lubricates particles at temperatures far below the melting temperature (Goldsby & Tullis 2002). Despite a relatively large range of uncertainties, contact shear strength is generally assumed to be severely damaged above $T_w = 1\,000$ °C (Goldsby & Tullis 2011). In contrast, quartz shows signs of melting at temperatures above 1650 °C (Lockner *et al.* 2017). Thus, we assume that flash heating only affects the frictional strength at the surface of the particles and that the particle itself remains in a solid state throughout the analysis (i.e. particle melting is not considered). This assumption is consistent with laboratory stick-slip experiments on dry bare-surface granite faults, showing that shear melting is mainly observed at much higher temperatures than the flash heating threshold and is driven by confining pressures above 200 MPa (Lockner *et al.* 2017). These stress values are far above the effective pressures in the seismogenic crust considered in this study.

2.4 Model set-up

The simulation of the seismic shear zone requires creating a numerical prototype dimensioned according to the geometric, kinematic, and dynamic conditions that prevail in the hypocentral zone of a shallow earthquake. To satisfy these conditions, we designed a numerical model in 2D similar to a rotary shear machine, consisting of a semi-periodic rectangular sample sheared in between two rigid walls (*cf.* Fig. 2, left). The semi-periodic condition enables modeling the growth of the shear zone without introducing lateral boundaries through a unit cell with dimensions of 2 mm × 1.5 mm, which represents a large (infinite) system. Two complementary boundary conditions are defined for the walls.

The top wall is subjected to a stress boundary condition in the vertical direction specified by an external force representing the effective confining pressure σ_n'. The vertical movement of the top wall is governed by its mass (equivalent to the granular sample mass) and by the resultant force acting on the wall, which includes the contact force applied by the sample located below. In contrast, the top wall is blocked horizontally, and it applies shear stress at the top of the granular sample.

The bottom wall is subjected to a velocity boundary condition in the horizontal direction and is blocked vertically. The slip velocity V_S is defined by a step function in which velocity passes from 0 to V_S in one time step (i.e. 10^{-5} ms), once the confining pressure is applied.

The numerical prototype represents a millimeter-scale rock volume composed of silt-sized dry particles, which presents a pre-existing fracture that induces strain localization during shear tests. The granular sample consists of 30 400 discs whose particle-size distribution is polydisperse, thus ensuring an isotropic behavior during the simulations. Particle diameters are uniformly distributed in the interval [$0.8\bar{d}$, $1.2\bar{d}$], where $\bar{d} = 0.01$ mm is the average disk diameter. Disk sizes are representative of average particle sizes observed in natural gouge zones and rotary shear tests of rock samples (An & Sammis 1994).

The construction of the sample follows several successive stages designed to create a highly dense granular material. Firstly, we prepare a dense geometric configuration by inserting particles one after another into the semi-periodic rectangular box using an algorithm minimizing the potential energy (Taboada *et al.* 2005). Secondly, the dense sample is compacted vertically to generate a granular material with very high relative density, whose mechanical behavior is representative of many rock materials with low porosity. During this stage, the sliding friction coefficient is set to zero (i.e. particle interactions are frictionless) to maximize the relative density of the sample. Thirdly, we activate the cohesive bonds within the top and

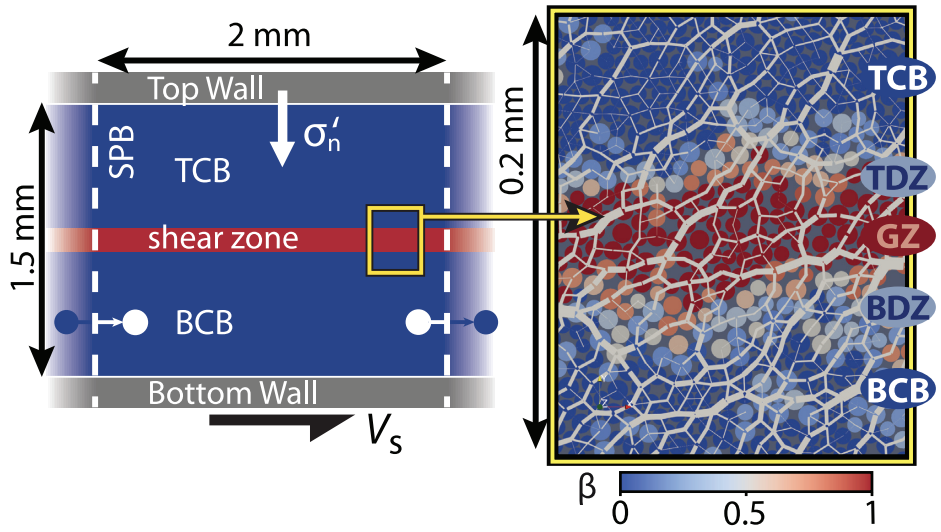

Figure 2. Left: Schematic drawing of the numerical shear test in which a semi-periodic sample of cohesive granular material traversed by a pre-existing fracture is located in between two rigid walls. The effective confining pressure σ_n' is applied on the top wall, whereas the slip velocity V_S is applied on the bottom wall. TCB: Top cohesive block; BCB: Bottom cohesive block. Right: Close-up of the granular sample around the shear zone showing the network of contact normal forces. Forces are represented by lines between particle centers, whose thickness is proportional to the force magnitude. Force chains are deviated in the gouge zone (GZ) and become subparallel to the shear zone due to the low shear strength. Particles are colored according to the average contact damage defined by the internal variable β (for $\beta = 0$, the cohesive bond is not damaged, whereas it is broken for $\beta = 1$). BDZ: bottom damage zone; TDZ: top damage zone.

bottom blocks, giving the two volumes a continuous character. Next, we simulate the pre-existing fracture by introducing a non-cohesive frictional law at the contacts between the top and bottom blocks. Lastly, we stabilize the sample to evacuate any parasitic movements linked to the transitions between the contact interaction laws.

As explained more fully in Section 3.1, the granular sample displays five superposed layers during the shear tests, defined according to the average damage at the particle scale (Berthier *et al.* 1988). For this purpose, we introduce a variable linked to the particle denoted β ($\beta \in [0, 1]$), representing the average cohesion intensity of the particle contacts. The close-up in Fig. 2 (right) illustrates the different layers of granular material as a function of β: The top and bottom cohesive blocks in which particles are interconnected by predominantly intact cohesive bonds ($\beta \in [0, 0.2]$), the top and bottom damage zones composed of particles with partially damaged bonds ($\beta \in [0.2, 0.8]$), and the gouge zone essentially composed of cohesionless particles ($\beta \in [0.8, 1]$). The layers' geometry and physical properties evolve as cohesive bonds are progressively damaged in the vicinity of the shear zone. Particles are abraded from the damage zones and incorporated into the gouge zone once their cohesive bonds break entirely. The abrasion process is controlled by the local texture and the distribution of contact forces that organize spontaneously in a strong and a weak network. This feature is illustrated in Fig. 2 (right), showing the network of normal contact forces whose orientations are deflected in the gouge zone (force magnitude is proportional to the thickness of the line joining particle centers).

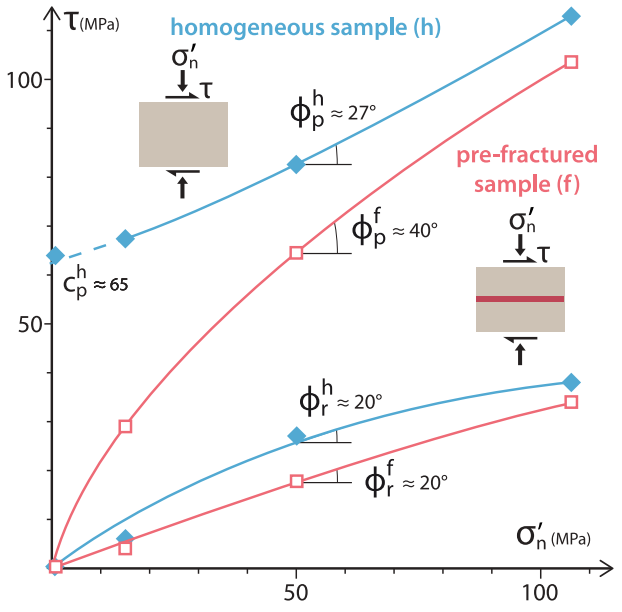

Figure 3. Peak and residual strength envelopes for cohesive granular samples determined from a set of numerical shear tests carried out under quasi-static conditions (slip velocity $V_S = 0.01$ m s^{-1}). The blue and red curves correspond to a homogeneous granular sample and a pre-fractured sample, respectively. Results from numerical tests for homogenous samples are indicated by filled diamonds and for pre-fractured samples by open squares.

2.5 Macroscopic strength of the granular material at low shear rate

Low-velocity shear tests were performed to determine the macroscopic shear strength of semi-periodic homogeneous and pre-fractured granular samples using the numerical prototype presented in the previous section. The pre-fractured sample is traversed by a pre-existing fracture, as indicated in Fig. 2, whereas the homogeneous sample is composed of a single cohesive block. We determined the peak and residual shear strengths for each sample type at four confining pressures (1.5, 15, 50 and 112.5 MPa) for a slip velocity of 0.02 m s^{-1}, one to two orders of magnitude smaller than earthquake slip velocities (*cf.* Fig. 3). We interpolated curves representing the samples' average peak and residual shear strengths

based on these data sets. These strength envelopes are compared with those for rocks to calibrate the granular material's macroscopic strength.

The peak strength envelope for the homogeneous sample is quasi-linear consistently with a Mohr–Coulomb failure criterion (Hackston & Rutter 2016). The peak cohesion and internal friction angle ($c_p^h \sim 65$ MPa and $\phi_p^h = 27^\circ$) are representative of values observed in shear tests for intact rocks (Hoek & Martin 2014). Contrastingly, the residual strength envelope for the homogeneous sample is defined by a concave-down increasing curve that passes through the origin, in agreement with the Hoek–Brown model. The residual friction angle decreases from $\sim 40^\circ$ at the origin to $\sim 5^\circ$ at the highest confining pressure (112.5 MPa). The degradation of the residual friction angle to values below the peak friction angle implies that the difference between peak and residual shear strengths increases with confining pressure.

Interestingly, the peak strength envelope for the pre-fractured sample is defined by a concave-down increasing curve that passes through the origin, as was also the case for the residual strength envelope of the homogeneous sample. The curvature of the envelope is similar to that of fractured rock masses determined from rock mechanics shear tests (Barton 2013). The peak friction angle ϕ_p^f decreases from $\sim 75^\circ$ at the origin to $\sim 30^\circ$ at the highest confining pressure. The residual strength envelope is slightly concave down with an average slope of $\phi_r^f \sim 20^\circ$. Thus, the Hoek–Brown model adequately describes the granular material's peak or residual strengths, both for pre-fractured or homogeneous samples that have already ruptured. Note that the peak and residual envelopes of both sample types converge for increasing confining pressures. This observation suggests that the effect of the pre-existing fracture tends to vanish at high confining pressures considering that the strength of the two samples becomes indistinct. In sum, the overall shape of strength envelopes for the granular material in the numerical models is in good agreement with experimental results from rock mechanics at low shear rates.

3 RESULTS

3.1 Sensitivity analyses of state variables during seismic shearing

We carried out two parametric studies to determine the rheology and physical properties of the shear zone for characteristic values of the state variables, namely the slip velocity, the confining pressure, and the flash-heating temperature. We summarize in the following section the results on shear zone evolution as a function of slip velocity and confining pressure. In turn, the parametric study concerning shear zone evolution as a function of the flash-heating temperature is presented in the supplementary material. Besides, for ease of reference, we synthesize in Tables 1 and S1 (supplementary material) the values of the state variables in the models for each parametric study.

The shear strength and the dilatancy of the shear zone are determined as a function of slip from the displacement field of the granular samples and the external stresses applied on the boundaries (i.e. the bottom and top walls). The analysis of the process of shear-zone formation is based on the calculation of the damaged zone located in between the two slipping blocks of cohesive granular material. The gouge zone grows as it incorporates wear debris (i.e. cohesionless particles) that are abraded from the surrounding damage zones. In this regard, a key element is the temperature distribution in the sample resulting from heat dissipation by friction. As shown further, shear coupling along the interphase between the damage and gouge zones partly controls the abrasion rate of particles. Shear coupling increases with the sliding friction coefficient of particles (Taboada *et al.* 2006), which sharply drops for temperatures close to T_w (*cf.* Fig. 1c).

3.1.1 *Effect of confining pressure and slip velocity*

The first parametric study focuses on the evolution of the shear zone as a function of confining pressure and slip velocity. To do so, we conducted a comparative analysis of four models by combining two values of normal effective stress σ_n' with two slip velocities (runs 1a–d, Table 1). The values of σ_n' are 112.5 and 56.3 MPa, which correspond to the effective lithostatic pressure at 7.5 and 3.75 km depth in the crust (e.g. considering an average unit weight of 24 kN m^{-3} for rock materials, a water table at the surface, and a hydrostatic pore pressure distribution at depth). The two pre-defined values for the slip rate are 0.5 m/s and 1 m s^{-1}, representative of average slip rates estimated for shallow earthquakes (Scholz 1998). The values of $\sigma_n' = 112.5$ MPa and $V_S = 1$ m s^{-1} (run 1d, Table 1) are termed hereafter as the reference model since they represent typical values observed in the hypocentral zone of shallow earthquakes.

The spatial and temporal evolution of the fault zone shows three phases controlled by the state variables, showing specific features (*cf.* Fig. 4):

1. A phase of rupture initiation (phase 1) in which the slip velocity imposed on the bottom wall jumps from zero to a positive constant value according to a step function. A well-marked peak in the frictional strength distinguishes this phase.
2. A transient phase of shear-zone growth (phase 2) in which frictional strength and dilatancy reach steady-state values at sub-melting temperatures.
3. A transient phase of thermal weakening (phase 3) in which the shear zone reaches a new steady-state regime at temperatures higher than the flash-heating threshold. This phase of dynamic shearing is characterized by a very low frictional strength (0.1–0.2) and a lower dilatancy value.

The main features of these phases are summarized below from the comparative analysis of the four models (see supplementary material for a detailed analysis of shear zone evolution during these phases).

Spectrograms calculated as a function of slip distance and time (x and t, *cf.* Fig. 5) illustrate the average evolution of damage and temperature (β and T) in the granular system. These graphs are generated from simulation values distributed in a regular grid comprising 400 columns and 80 lines. Columns represent the successive states of the system defined at constant intervals of 0.025 mm of slip (equivalent to 2.5 particle diameters). The spectrogram value associated with a node in the grid represents the average damage or temperature at a fixed state of the granular system, inside a horizontal stripe centered along the vertical line coordinate (the stripe width is 0.018 mm, or two particle diameters).

The initial and flash-heating temperatures in the models are set to $T_0 = 300$ °C and $T_w = 500$ °C, respectively. The meaningful parameter for simulations is the difference between initial and flash-heating temperatures ($\Delta T = 200$ °C) and not absolute temperatures since the shear strength weakens when particle contacts reach the flash-heating temperature. Note that the temperature difference is three times lower than in natural conditions (i.e. 300 °C is the

Table 1. Summary of variables used in runs for the parametric study I focused on the evolution of the shear zone as a function of confining pressure and slip velocity. The initial temperature T_0 is equal to 300 °C for all runs.

Parametric study	I			
Run variable	1a	1b	1c	1d*
Slip velocity V_S (m s^{-1})	0.5	1	0.5	1
Confining pressure σ_n (MPa)	56.3	56.3	112.5	112.5
Weakening temperature T_w (°C)	500	500	500	500
$\rho_{wall}/\rho_{sample}$	1	1	1	1
Slope of velocity function (m s^{-2})	10^8	10^8	10^8	10^8
Figures	4-8	4, 5	4-8	4, 5

Note: * reference model in the text.

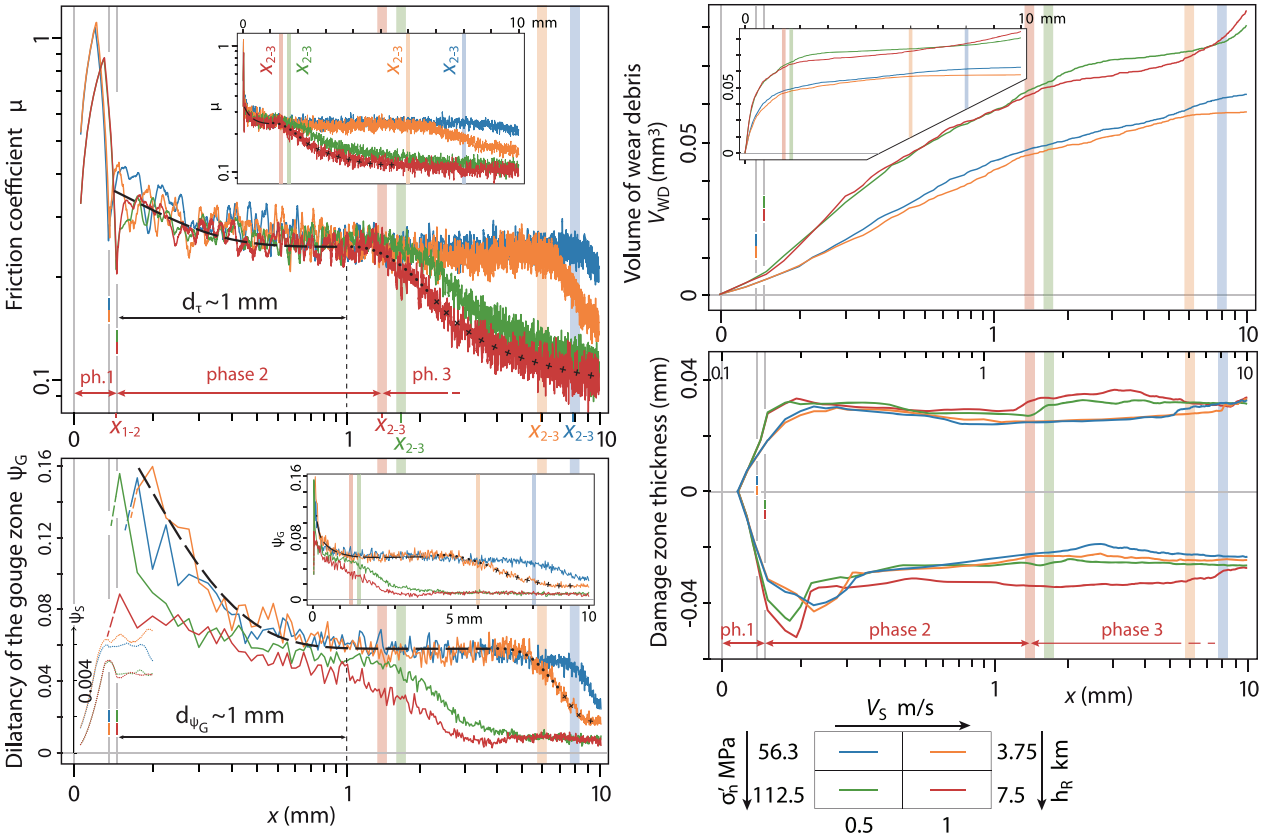

Figure 4. Strength, physical, and geometrical parameters of the shear zone and the granular sample as a function of slip distance x for two values of effective confining pressure and slip velocity (σ_n' and V_S) (runs 1a–d, Table 1). According to mechanical behavior, curves show three distinct phases (bounded by vertical color lines and stripes): Phase 1 of rupture initiation, phase 2 of shear-zone growth at submelting temperatures, and phase 3 of shear-weakening at flash-heating temperatures. Dashed curves are exponential approximations of friction and gouge dilatancy. The sigmoidal approximation curves for friction and dilatancy in phase 3 are plotted with dots and cross symbols (concave and convex segments, respectively). x_{1-2}: slip distance at transition between phases 1 and 2; x_{2-3}: onset of thermal weakening; h_R: height of the rock column (in km) corresponding to the effective confining pressure; d_τ, d_{Ψ_G}: critical decay distances for shear stress and gouge dilatancy, respectively. Ψ_S: sample dilatancy.

temperature of the base of the mechanical upper crust, while 500 °C is much lower than the flash-heating temperature of silicate minerals Burov 2011). This choice enables addressing the main processes involved in shear-fault evolution while limiting the computation time that can be excessively long (higher flash-heating temperatures require longer slip lengths).

The average thickness of the damage zones is estimated from the damage spectrograms. We define the damage zone thickness as the vertical distance between contour lines $\beta = 0.2$ and $\beta = 0.8$ in the spectrograms. Note that the average damage value near the gouge-damage zone interface represents an average sum, including particles within cohesive asperities (with low to intermediate damage values) and cohesionless particles located in the troughs between asperities (with maximum damage).

The friction coefficient along the shear zone is calculated from the ratio between the normal and shear stresses applied on the top and bottom walls of the granular system. Friction curves are smoothed by plotting their moving average taken over a 0.015 mm slip distance interval ($1.5\bar{d}$).

Dilatancy values calculated in the shear zone and at sample scale characterize volume changes during the shear tests. Dilatancy is defined as the average expansion of the granular material relative

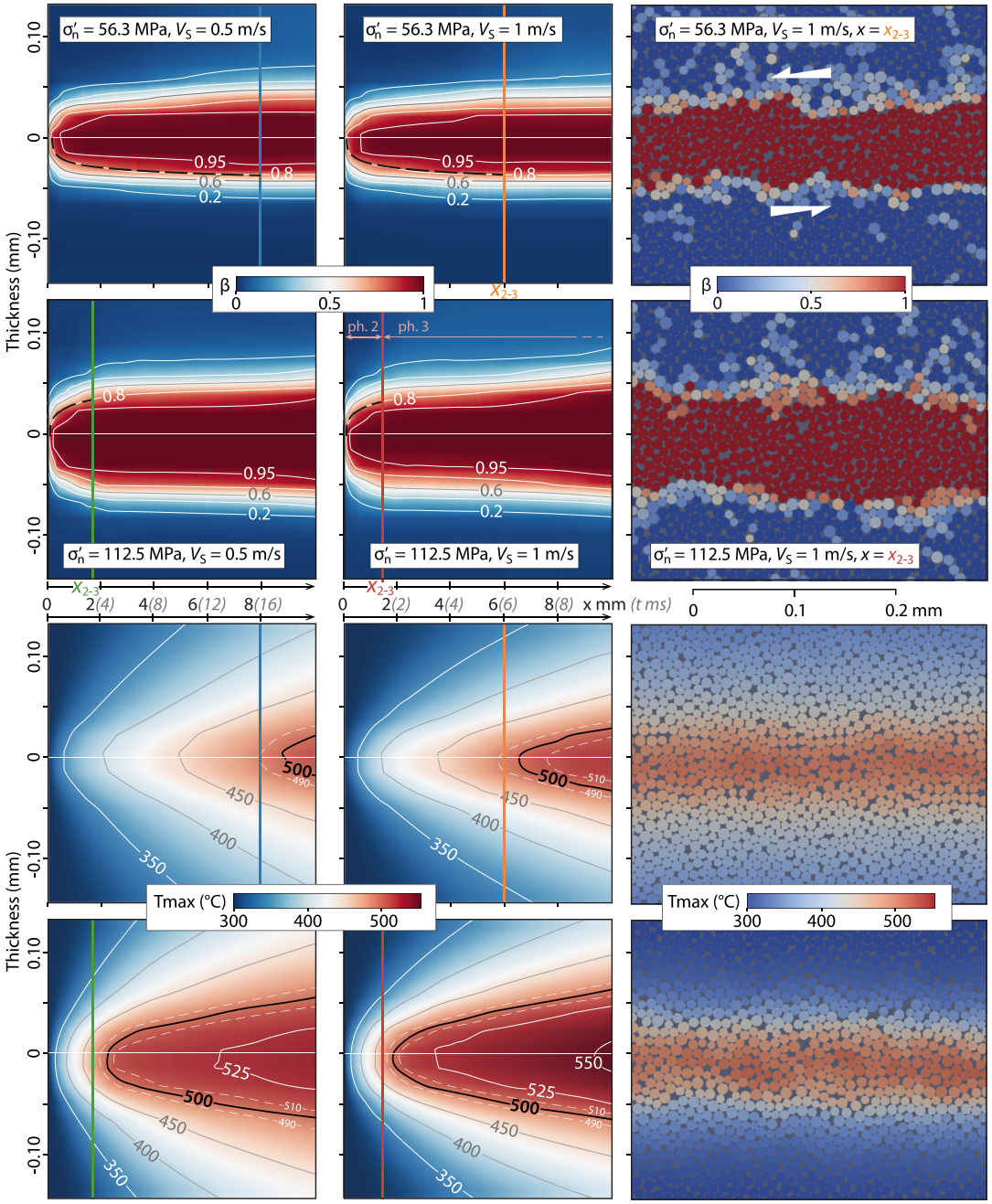

Figure 5. Spectrograms calculated as a function of slip distance or time (x and t) illustrating the average evolution of damage and temperature (β and T) in the shear zone for two values of effective confining pressure and slip velocity (the time scale is indicated in brackets) (runs 1a–d, Table 1). The average state of the granular sample at a given slip distance is represented by a vertical profile obtained by calculating average values of parameters within thin horizontal slices. Vertical color lines indicate the onset of thermal weakening (x_{2-3}); dashed curves are logarithmic approximations of contour level $\beta = 0.8$, bounding the gouge zone. The right column shows a microscale view of the shear zone for slip distance x_{2-3}.

to its position in the initial state once the confining pressure is applied (i.e. $\Delta h/h_0$, where h_0 is the initial thickness of the layer in question). We measure dilatancy within the shear zone, defined as the area in which average damage is greater than a threshold ($\beta > 0.6$). Note that this area includes the gouge zone and a thin layer of the adjacent damage zones. The shear zone dilatancy is termed Ψ_G since it primarily represents the expansion of the gouge zone. Secondly, we calculate for phase 1 the average dilatancy of the granular sample as a whole (termed as Ψ_S). This parameter enables to readily identify volume changes during rupture initiation.

As explained in the supplementary material, the average evolution of the granular system is independent of specific values of boundary conditions such as the mass of top wall or the slope of the step function defining slip velocity.

3.1.2 *Phase 1 of initiation of rupture*

The two blocks of cohesive granular material in contact along a pre-existent discontinuity, are successively pressed together by the confining pressure and sheared abruptly by imposing a velocity step function on the bottom wall. The velocity step triggers a very short phase of rupture initiation, which exhibits specific features in physical and mechanical parameters as follows (*cf.* Fig. 4).

The overall shape of the friction curves in phase 1 can be approximated by a left skew (asymmetric) peak function, which sharply increases from the origin to a maximum strength value close to 1, and then drops sharply to a minimum residual strength value. Within the range of values for the state variables, the frictional strength, dilatancy and volume of wear debris, are primarily controlled by the normal stress. These parameters are almost independent of slip velocity. The phase of rupture initiation involves low temperatures far below the flash-heating threshold and brittle deformation regime in the shear zone (further details in the supplementary material).

3.1.3 *Phase 2 of shear-zone growth at submelting temperatures*

After the local minimum in the shear strength, the shear zone enters a new transient phase in which its thickness increases, while friction decreases asymptotically with slip distance (*cf.* Fig. 4). The average gouge thickness can be estimated from the damage spectrograms (*cf.* Fig. 5): It is assumed that the boundary between the gouge and the damage zones follows the contour line $\beta = 0.8$. According to this criterion, the gouge zone consists of particles having lost more than 80 per cent of their cohesive bonds. Spectrograms show that the average gouge width increases at a decreasing rate with slip distance. In a first-order approximation, gouge width can be estimated by logarithmic curves that fit contour line $\beta = 0.8$.

Average friction for the four case studies falls from a maximum value of ∼0.35 for very low slips to a minimum value of ∼0.25 for slips between 1.5 and 8 mm (cf. Fig. 4). Constrastingly, the volume of wear debris and the thickness of the gouge zone are primarily controlled by confining pressure (and not slip velocity). Hence, doubling the normal stress induces a net increase in the thickness of the gouge zone (i.e. $\beta \geq 0.8$), which passes from 6 to 9 particle diameters at the end of phase 2 (*cf.* Fig. 5, right column). This trend is consistent with higher normal and shear forces at cohesive contacts, susceptible to increment plastic deformation inside the damage zone. Note that the maximum average friction observed at the start of phase 2 is associated with the maximum gouge thickening rate.

Many studies show that in dynamic granular systems, the friction coefficient in a steady-state regime is an increasing function of a dimensionless shear rate named the inertial number $I = \dot{\gamma}\bar{d}\sqrt{\rho/P}$, where $\dot{\gamma}$ is the average shear rate, $\bar{d}$ is the average particle diameter, P is the pressure, and ρ is the density (GDR MiDi 2004; Koval *et al.* 2009). However, doubling the slip velocity induces a slight decrease in friction, which is unexpected, considering that the shear rate and the inertial number should also double. We recall that the average shear rate $\dot{\gamma}$ is defined as the ratio between shear velocity and thickness of the shear zone. Thus, the average steady-state value of the shear rate in the first parametric study (runs 1a–d, Table 1) is between 5×10^3 and 15×10^3 s^{-1}.

For the four case studies, shearing occurs under quasi-static conditions in which dynamic effects are not significant. As a result of high confining pressures and small particle sizes, the inertial number is lower than 10^{-3}, even if the seismic shear rates considered in the models are high (Parez *et al.* 2021). Additionally, the frictional strength in quasi-static shear flow grows very slowly with the inertial number (Peyneau & Roux 2008). We infer that friction is roughly constant for the range of inertial numbers considered in this study. The increase in shear zone thickness resulting from doubling the confining pressure reduces the average shear rate and the inertial number. This reduction, in turn, is consistent with the slight decrease in dilatancy and frictional strength shown in the curves in Fig. 4 (red and green curves compared to orange and blue curves).

The effect of the velocity step function is apparent in the formation of the damage zones that bound the gouge zone (*cf.* Fig. 4). The thickness of the bottom damage zone shows a well-marked peak for very low displacements, which occurs during phase 2, right after the initiation of the shear rupture. After the peak, the thickness of the damage zones stabilizes around steady values (between 2 and 3 particle sizes). Note that the state variables (pressure and slip velocity) and the rate of abrasion have only a minor influence on the thickness of the damage zone. Thus, asperities at granular scale with similar heights are progressively renewed. Their lifetime is controlled by shear coupling between the rough interfaces and the cohesionless gouge material.

The volume of wear debris can be approximated by two logarithmic curves (the two linear segments in the semi-log plot of Fig. 4) with similar coefficients correlated with the deformation process in the shear zone during phase 2. The slightly steeper line segment observed at the beginning of phase 2 indicates a more active abrasion regime during the transient response of the granular sample, successive to the damage zone thickness peak. The logarithmic trend derived from our models indicates that the wear rate (i.e. the slope of the curve) decreases from very high values during the phase of rupture initiation to low values that tend toward zero when the shear zone reaches the steady state at submelting temperatures.

Phase 2 extends over a slip distance that varies according to the specific model (x_{2-3}, indicated by vertical color stripes, Figs 4 and 5). This distance delimits the transition between phases 2 and 3, which is controlled by the shear zone's thermal evolution. Heat dissipation and temperature rise mainly depend on confining pressure and, to a lesser extent, on slip velocity (*cf.* Fig. 5) (further details in the supplementary material).

3.1.4 *Phase 3 of shear-weakening at flash-heating temperatures*

This phase is characterized by a transient state in which frictional strength tends asymptotically to a very low value at temperatures higher than the flash-heating threshold (cf. Fig. 4). More precisely, friction can be approximated by asymmetrical sigmoidal curves that join horizontal asymptotes. The slip interval in each model is defined between the vertical color stripe (or color line in spectrograms in Fig. 5) and the maximum slip displacement ($x_{2-3} - 10$ mm). The friction coefficient decreases from the previous plateau in phase 2 to a thermally weakened threshold close to 0.1. Note that 0.1 is the macroscopic frictional strength of frictionless granular samples sheared under quasi-static conditions (Peyneau & Roux 2008), in line with the low contact friction coefficient defined for particles in the gouge. This trend is clearly identified in high-pressure simulations (red and green curves in Fig. 4). In contrast, only the transient state is plotted for intermediate-pressure simulations (blue and orange curves) since flash heating occurs for slip distances greater than 10 mm.

At the beginning of phase 3, the volume of wear debris can be approximated by a linear segment in the semi-log plot (*cf.* Fig. 4),

either horizontal (i.e. intermediate pressure, orange curve) or gently sloping (i.e. high pressure). This behavior is consistent with the damage spectrograms indicating that for intermediate confining pressure, the thickness of the gouge zone reaches a constant value (i.e. the contour line $\beta = 0.8$ is horizontal) (*cf.* Fig. 5). In contrast, the thickness increases at a very low rate for high confining pressure (i.e. according to a logarithmic trend). Granular material at the start of phase 3 can be classified into three mechanical states, based on damage intensity level: The cohesionless gouge located inside the shear zone (red particles), the cohesive blocks in the top and bottom blocks (blue particles), and the damage zones that are composed of particles with partially damaged bonds (light red to light blue particles) (*cf.* Fig. 5, top, right column). The peripheral fringe separating red from light-colored particles delimits the boundary between the damage zones and the gouge. The waviness of this interface (i.e. its roughness) is apparent, showing that asperities in the top and bottom damage zones have more or less asymmetric shapes.

Phase 3 is characterized by a new steady-state regime defined by lower values of friction and dilatancy (*cf.* Fig. 4). The dilatancy of the gouge zone (Ψ_G) in phase 3 is also defined by sigmoidal curves bounded by horizontal asymptotes (e.g. orange curves in the semi-log and linear plots, Fig. 4). However, they are not asymmetric, as observed for friction. Steady-state dilatancy in phase 3 is slightly lower for high than for intermediate confining pressure, as observed in phase 2. The average damage zone thickness is fairly constant during the weakening phase due to low abrasion rates (further details in the supplementary material).

3.2 Breakdown energy during rupture initiation

In this section, we calculate the breakdown energy consumed to generate the gouge material and damage zones during rupture initiation as a function of confining pressure and compare it with the fracture energy commonly used in seismology as a proxy of coseismic on- and off-fault damage (Kanamori & Rivera 2006). For this purpose, we have selected two case studies from the first sensitivity analysis at intermediate and high confining pressures ($\sigma_n' = 56.3$ and 112.5 MPa, respectively) (runs 1a and 1c, Table 1). The slip velocity and weakening temperature are the same for both case studies ($V_S = 0.5$ m s^{-1} and $T_w = 500$ °C).

Breakdown energies are compared to fracture energies at the end of transient regimes in phases 2 and 3, representing steady states in brittle and thermally-weakened strain regimes, respectively. For this purpose, we use the generalized definition of fracture energy broadly used in seismology, determined by the post-failure integral of the dynamic weakening curve (Abercrombie & Rice 2005):

$$\Gamma(x) = \int_0^x (\tau(u) - \tau(x))du, \tag{5}$$

where $\tau(x)$ is the shear strength applied on the bottom wall as a function of slip. Note that this expression is frequently applied to calculate the fracture energy in high-velocity friction experiments on rock samples (e.g. Passelègue *et al.* 2016b). Fracture energies for the two phases and case studies are $\Gamma_1^{p2} \sim 3.6$ mJ, $\Gamma_2^{p2} \sim 2.4$ mJ, $\Gamma_1^{p3} \sim 70$ mJ and $\Gamma_2^{p3} \sim 40$ mJ, where the index and exponent represent the case study and the phase number, respectively.

We calculate breakdown energies at cohesive bonds from the behavior laws defining strength at the contact scale (Section 2.2). This requires decomposing the contact shear force into a cohesive and frictional component: $T_c = T_c^C + T_c^\mu$ (*cf.* Fig. 1a). The work done by contact forces to break down a cohesive bond comprises a decohesion component w_c^C and a debonding frictional component w_c^μ. The decohesion energy per bond, defined as $w_c^C = w_c R_e$, corresponds to the elastic energy released when a cohesive bond breaks in shear or traction modes. According to the setting of model parameters, $w_c C = 0.2\,\mu$J for average size particles, regardless of confining pressure.

Likewise, the average debonding frictional energy per bond is defined by $w_c^\mu = \delta_c T_c^\mu$, where $T_c^\mu = \mu_s N_c$ is the frictional component of shear force, μ_s is the local sliding friction coefficient, and N_c is the normal contact force. We suppose that the rupture of cohesive bonds results mainly from sliding (not from rolling) of particles as particle rolling is constrained within the cohesive granular material. This hypothesis may lead to a minor overestimation of the debonding frictional energy as some rolling may occur during the rupture process. Unlike the decohesion energy, w_c^μ is proportional to contact shear force and may vary during the shear test (average values at submelting temperatures for the two case studies are $w_{c2}^\mu = 2w_{c1}^\mu = 0.23\,\mu$J). Note that debonding frictional energy is different from the frictional energy dissipated by cohesionless particles in the gouge zone.

3.2.1 Breakdown energy of the gouge zone

The breakdown energy W_G consumed to generate the gouge zone from intact cohesive granular material results from the additive effect of work done against cohesive and frictional contact forces and from shear-induced dilatancy: $W_G = W_G^C + W_G^\mu + W_{\Psi_G}$, where W_G^C is the decohesion energy of gouge particles, W_G^μ is the debonding frictional energy of gouge particles, and W_{Ψ_G} is the work associated to the dilatancy of the gouge zone (i.e. work done against confining pressure) (Makedonska *et al.* 2011). The debonding energies are equally distributed between the two particles in contact.

During rupture initiation, the breakdown energy of the gouge zone and its components (W_G^C, W_G^μ and W_{Ψ_G}) show a transient regime for the two case studies, which exhibits specific features when the confining pressure doubles (i.e. from $\sigma_n' = 56.3$ to 112.5 MPa) (*cf.* Fig. 6, top):

1. At the end of the transient regimes, W_G roughly doubles (from ∼0.64 to ∼1.2 mJ mm^{-2}), suggesting that for brittle behavior, W_G is quasi-proportional to σ_n'.
2. However, at this stage, the relative contribution of the three energy components to the total energy W_G (i.e. the relative size of colored circles in each plot) does not vary homogeneously with confining pressure. Notably, the relative contribution of decohesion energy W_G^C (yellow circles) decreases by ∼60 per cent, consistently with the reduction of the relative contribution of cohesion to shear strength as σ_n' increases (*cf.* Section 4.4). On the other hand, the relative contribution of debonding frictional energy W_G^μ (pink circles) and dilatancy energy W_{Ψ_G} (blues circles) increases with σ_n' by ∼40 per cent and ∼15 per cent, respectively. Thus, according to these results, decohesion and dilatancy are the primary energy sinks linked to gouge formation at intermediate pressures. In contrast, dilatancy and debonding frictional energies predominate at high confining pressures.
3. W_G grows with slip displacement, following concave down curves that decay over critical distances (d_G) that decrease by one-third when doubling the confining pressure. These curves can be approximated by logarithmic or exponential functions (dotted and dashed gray curves). The logarithmic curve is consistent with a positive wear rate in steady-state conditions. In contrast, the exponential curve suggests that the wear rate tends to zero as the gouge zone

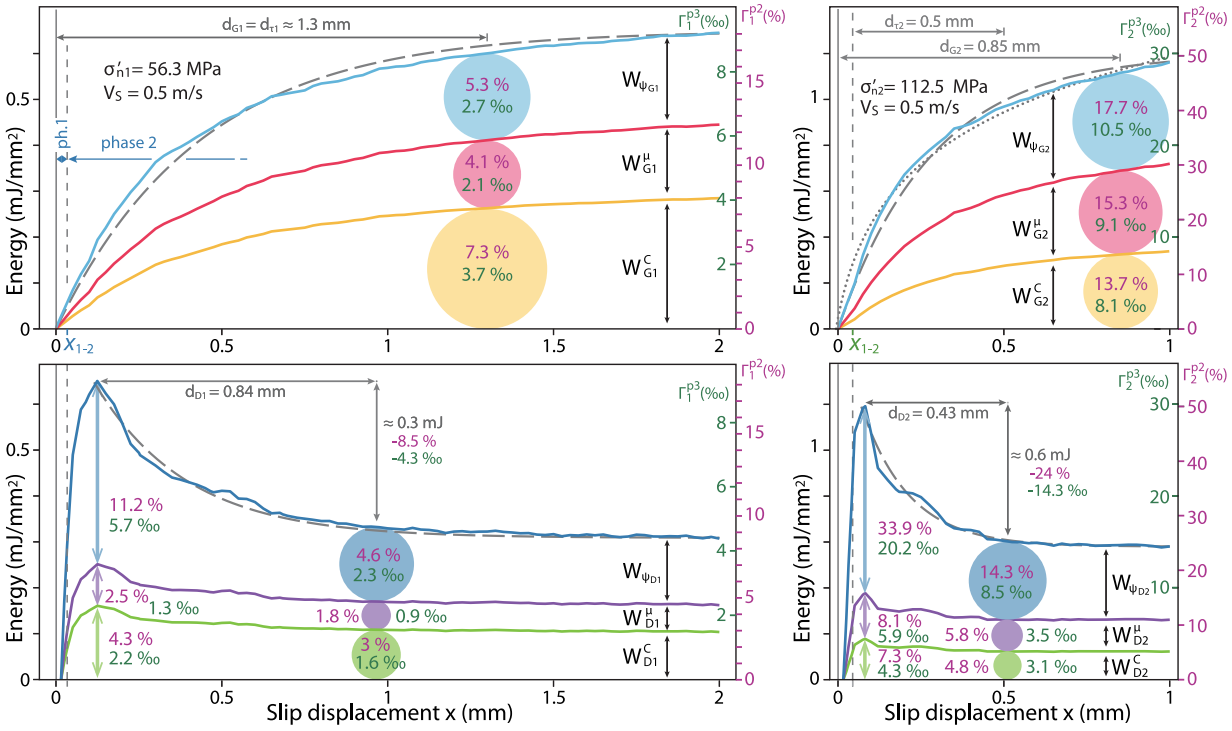

Figure 6. Cumulative curves illustrating the breakdown energy components for the gouge material (top) and damage zones (bottom) as a function of slip displacement (runs 1a and 1c, Table 1). Intermediate and high confining pressures are labeled with indexes 1 and 2 (left and right plots), respectively. W_G^C, W_G^μ, W_{Ψ_G}: Decohesion energy, debonding frictional energy, and dilatancy energy for the gouge zone (yellow, red and light blue curves, respectively). W_D^C, W_D^μ, W_{Ψ_D}: Decohesion energy, debonding frictional energy, and dilatancy energy for the damage zones (green, purple and blue curves, respectively). The relative magnitude of energy components at the critical decay distance is given by the size of the corresponding colored circles. Γ^{p2}, Γ^{p3}: Fracture energies at the end of transient regimes in phases 2 and 3, respectively (i.e. representing brittle and thermally-weakened strain regimes). Fracture energy values are defined inside colored circles according to the pink and green scales. d_τ, d_G, d_D: Critical decay distances for shear stress and breakdown energies of gouge and damage zones, respectively. Dashed and dotted curves are exponential and logarithmic approximations of energy curves.

thickness reaches a threshold value (*cf.* Fig. 6). At intermediate confining pressure, the critical decay distances for gouge breakdown energy and shear stress are similar ($d_{G1} \approx d_{\tau 1} \approx 1.3$ mm). Contrastingly, both distances are sub-millimetric at high confining pressures, with $d_{G2} \gg d_{\tau 2}$ indicating that active abrasion continues during the steady-state regime for frictional strength (*cf.* Section 4.3).

Several relations can be proposed between energy components and other parameters of the gouge layer when doubling the confining pressure, which are valid in particular at the end of the transient regimes (i.e. for $x_1 \sim d_{G1}$ and $x_2 \sim d_{G2}$):

1. The ratios of decohesion energies, wear debris volumes, and gouge thicknesses are roughly equal (Figs 4-6):

$$W_{G2}^C / W_{G1}^C \sim V_{WD2} / V_{WD1} \sim H_{G2} / H_{G1} \sim 1.2, \quad (6)$$

This relation suggests that W_{G2}^C is quasi-proportional to gouge thickness H_G, which is 20 per cent greater for high confining pressure.

2. The ratio of debonding frictional energies is roughly proportional to the product of the ratios of confining pressure and gouge thickness:

$$W_{G2}^\mu / W_{G1}^\mu \sim \sigma'_{n2} / \sigma'_{n1} . H_{G2} / H_{G1} \sim 2.4, \quad (7)$$

This relation is consistent with the increase in the frictional component of contact shear forces T_C^μ with σ'_n (*cf.* Fig. 1a).

3. The ratio of dilatancy energies more than doubles ($W_{\Psi_{G2}} / W_{\Psi_{G1}} \sim 2.2$) as it is also proportional to the ratios of σ'_n and H_G. However, gouge dilatancy in steady-state conditions is lower for high confining pressure ($\Psi_{G2} / \Psi_{G1} \sim 0.9$), proportionally reducing $W_{\Psi_{G2}}$.

4. The ratio of gouge breakdown energy to fracture energy in phase 2 (W_G / Γ^{p2}) nearly triples, indicating that W_G becomes the dominant component of Γ^{p2} at high confining pressures (pink scale, Fig. 6). The above-cited ratio grows from ∼18 per cent to ∼50 per cent when doubling σ'_n. In contrast, the ratios of the breakdown energy components to fracture energy vary non-uniformly (*cf.* percentage values in pink plotted inside circles, Fig. 6). These values are globally higher for high σ'_n because W_G roughly doubles, whereas the fracture energy decreases by one-third.

5. The ratio of gouge breakdown energy to fracture energy in phase 3 (W_G / Γ^{p3}) more than triples, yet W_G remains below a few percent of Γ^{p3} (permille values, green scale, Fig. 6). The above-cited ratio grows from ∼8.5‰ to ∼28‰ when doubling σ'_n. As for Γ^{p2}, the ratios of the breakdown energy components to fracture energy vary non-uniformly (cf. values in green plotted inside circles, Fig. 6). Accordingly, these values are globally higher for high σ'_n because W_G roughly doubles, whereas the fracture energy decreases by ∼43 per cent.

3.2.2 *Breakdown energy of the damage zone*

As for the gouge zone, the breakdown energy W_D consumed to generate the damage zones from intact cohesive granular material results from the additive effect of equivalent terms calculated for the partially damaged granular material: $W_D = W_D^C + W_D^\mu + W_{\Psi_D}$.

We suppose that damaged particles' decohesion and debonding frictional energies (W_D^C and W_D^μ) are proportional to damage β, which measures the average mechanical degradation of the cohesive bonds (*cf.* Section 2.4). The dilatancy energy W_{Ψ_D} integrates the work done against confining pressure for the top and bottom damage zones.

During rupture initiation, the breakdown energy and its components (W_D^C, W_D^μ and W_{Ψ_D}) show a transient regime for the two case studies, which exhibits specific features when the confining pressure doubles (i.e. from $\sigma_n' = 56.3$ MPa to 112.5 MPa) (*cf.* Fig. 6, bottom):

1. The energy W_D shows a well-marked peak during phase 2 right after the initiation of the shear rupture, whose magnitude roughly doubles from $\sim$ 0.63 to $\sim$ 1.2 mJ mm^{-2}. These energy values are similar to those for W_G at the end of the transient phase, suggesting that the velocity step imposed on the bottom wall induces intense damage in cohesive material adjacent to the fault surfaces.

2. After the peak, W_D decreases exponentially by one-half to steady-state values, over critical distances shorter than the critical distance for the gouge energy decay ($d_D < d_G$). Thus, the initial thickness of the damage zone decreases substantially, reaching the steady-state condition before the gouge zone thickness stabilizes (cf. Fig. 4 and 5).

3. The dilatancy energy component W_{Ψ_D} (dark blue arrows and circles, Fig. 6) is equivalent to $\sim$ 2/3 of the energy peak and $\sim$ 1/2 of the steady-state value, indicating that dilatancy is the primary energy sink within the damage zones. Initial shearing involves cracking and dilation of cohesive granular material within asperities at intermediate and high confining pressure. The remaining energy ($\sim$ 1/3 and $\sim$ 1/2 of W_D) corresponds to the sum of the decohesion and debonding frictional energies (green and purple arrows and circles, Fig. 6).

4. The relative proportion of decohesion and debonding frictional energies in steady state ($\sim W_D/2$ is considerably less than for the gouge zone because particle bonds are partially broken.

5. However, as for the gouge zone, the relative proportion of decohesion energy in steady state decreases with σ_n', whereas that of debonding frictional energy grows.

6. The ratio of damage zones breakdown energy to fracture energy at steady state in phase 2 (W_D/Γ^{p2}) nearly triples, growing from $\sim$ 9 per cent to $\sim$ 25 per cent when doubling σ_n' (pink scale, Fig. 6). Accordingly, the ratio of damage breakdown energy to fracture energy at steady state in phase 3 (W_D/Γ^{p3}) more than triples, yet W_D remains below a few percent of Γ^{p3}, growing from $\sim$4.4‰ to $\sim$14‰ when doubling σ_n' (permille values, green scale, Fig. 6).

4 DISCUSSION

4.1 Frictional strength

The general shape of friction curves obtained in our numerical tests is similar to that obtained in many experimental tests on bare rock surfaces sheared at high velocities and variable confining pressures (Hirose & Shimamoto 2003; Di Toro *et al.* 2004; Reches & Lockner 2010; Goldsby & Tullis 2011; Proctor *et al.* 2014; Passelègue *et al.* 2016b). There are, however, differences in the peak and residual frictions and the critical slip distances for frictional and dilatancy decay at submelting and flash heating temperatures (critical distances are defined as the slip displacement corresponding to the 95 per cent reduction from peak to steady-state values).

The peak friction values induced by the velocity step ($\mu_p = 0.9$ and 1.1, Fig. 4) are slightly higher than those observed in experimental tests on bare rock surfaces (0.6–0.95) (cf. above-cited studies). Higher values in numerical tests are linked to specific differences between rock samples and cohesive granular materials considered in the simulations. Firstly, particles in our models are rigid and cannot fracture, increasing dilatancy and shear strength upon shearing. The contribution of dilatancy to the shear strength in 2D models increases linearly with the contact friction angle (Taboada *et al.* 2006). Secondly, the two mating surfaces along the shear plane are perfectly matched since they are obtained by deleting cohesive bonds between particles in contact on opposite sides of the pre-existing fracture (*cf.* Fig. 1). This last condition is never wholly achieved in experimental rock samples, which are ground to specific values of flatness and roughness that modify the surface roughness and the size and shape of asperities in the mating surfaces (McLaskey *et al.* 2012; Mitchell *et al.* 2013). Contrastingly, natural faults display rough surfaces at small scales that may substantially increase the local shear strength (Brodsky *et al.* 2016).

An increase in the slope of the slip velocity function (i.e. the shear acceleration) does not affect the peak friction. Instead, it slightly reduces the corresponding slip distance to values between 3 and 5 particle diameters (cf. Fig. S6, supplementary material). This slip distance can be identified with the average wavelength of the asperities (surface summits) located between the mating surfaces that are abraded or sheared off during the triggering of the shear instability (*cf.* animation file in supplementary material). Peak frictions are comparable to those obtained in similar numerical shear tests performed at low slip velocities (Guo & Morgan 2008). Accordingly, peak frictions measured in high-velocity shear tests are steady for an extensive range of shear accelerations (10−250 m s^{-2}) (Chang *et al.* 2012; Proctor *et al.* 2014; Barbery *et al.* 2021).

The residual friction values at submelting temperatures ($\mu_r \sim$ 0.25, Fig. 4) are smaller than those observed in high-velocity shear tests on bare rock surfaces (Proctor *et al.* 2014), which are closer to those predicted by Byerlee's friction law ($\mu_r \sim 0.6$). This feature is linked to dimensional and geometric factors specific to our model. Firstly, dense packings of 2-D discs have lower frictional strengths than equivalent 3-D sphere packings due to the increasing coordination number inherent to 3-D models (Frye & Marone 2002). Secondly, granular assemblies of circular (or spherical) particles have lower frictional strengths than polygonal assemblies as contact forces do not exert resisting torques (Estrada *et al.* 2008). Accordingly, numerical tests show that shearing of disk assemblies involves mechanisms such as vorticity cells assisted by rotational bearings and localized rolling of a thin granular layer, which reduce the frictional strength (e.g. $\mu_r \sim 0.3$ for $\mu_s < 0.9$) (Alonso-Marroquín *et al.* 2006; Makedonska *et al.* 2011).

Asymmetrical sigmoidal decreasing curves can represent friction during the transient stage of thermal weakening (phase 3, Figs 4 and S1 in supplementary material). Likewise, sigmoidal shear strength decay has been proposed during the coseismic stages of fault slip due to crystal plastic deformation of quartz during the very initial stages of fault slip (Bestmann *et al.* 2012). The shape of the sigmoidal curves in our numerical models is presumably correlated with the hyperbolic tangent function representing the decrease of contact friction over a reference temperature interval of $2T_v$ centered around the thermal weakening temperature T_w (*cf.* Fig. 1c). However, the sigmoidal shape contrasts with the exponential decreasing function traditionally used to approximate frictional decay during thermal weakening in high-velocity shear experiments (Hirose & Shimamoto 2005; Di Toro *et al.* 2011). In particular, the

exponential approximation cannot fit the sub-millimetric convex curve segment located around slip distance x_{2-3}, where friction decreases by ∼30 per cent of the stress drop (dotted curves, Figs 4 and S1 in supplementary material). Flash heating induces dramatic weakening of the friction coefficient (>40 per cent) after a few millimeters of slip (Spagnuolo *et al.* 2016), almost independently of rock type. The mismatch between curve shapes may be linked to unrealistic boundary conditions present in most high-velocity experiments using rotary apparatus, in which gouge created by wear of the rock surfaces is partially extruded from the slip surface (Reches & Lockner 2010; Kuo *et al.* 2015). Note that gouge extrusion will constantly reset the heat stored around the slip zone (Nielsen *et al.* 2021), artificially modifying the thermal evolution and the abrasion rate in the shear zone and increasing the slip distance required for flash heating. Even so, the average initial trend of friction curves in the transient weakening stage is still consistent with thermal softening of friction observed in high-velocity shear tests at high normal stresses and predicted by numerical models (Aharonov & Scholz 2018).

Slip velocities in our simulations are much higher than the cutoff slip rate (∼1 mm s^{-1}), above which contact growth or strengthening of asperity contacts between sliding surfaces is insignificant (Dieterich 1978; Nakatani & Scholz 2006; Noda 2008; Aharonov & Scholz 2018). Thus, the "state evolution effect" (or direct velocity effect), linked to the aging of asperity contacts, can be neglected and was not introduced in the particle contact law (i.e. particle surface friction at submelting temperatures is constant, $\mu_s = 0.5$, cf. Section 2.2). Conversely, the constitutive formulations of rate-and-state friction (RSF) traditionally introduce these effects as they exert significant control on strength evolution at low slip rates (Dieterich 1978; Ruina 1983; Marone 1998; Baumberger & Caroli 2006).

The RSF laws are a central component of multi-asperity models, in which the shear zone is represented by an effective rough surface (a superposition of two rough profiles or surfaces) characterized by an ensemble of frictional asperities (surface summits) (Bowden & Tabor 1964; Greenwood & Williamson 1966; Dieterich & Kilgore 1994; Persson 2001; Rubinstein *et al.* 2004; Vakis *et al.* 2018). It is worth noting that this model breaks down once a gouge layer of wear debris forms between the damaged surfaces since the shear strain is distributed within a volume of particles (and not localized in between two surfaces). The intrinsic difference between multi-asperity and granular models can be illustrated by comparing the critical slip distance d_τ required to reach steady-state conditions. In multi-asperity models, d_τ is often interpreted as being close to an asperity size (∼1–10 μm). Contrastingly, the critical distance required to generate a gouge zone with a critical thickness in discrete element models is two orders of magnitude greater than asperity sizes (cf. Fig. 4). As explained in Section 3.2, the transient frictional strength in phases 1 and 2 is closely related to the breakdown energy consumed to create the damage and gouge zones.

4.2 Gouge zone thickness

The thickness of the gouge zone H_G at submelting temperatures roughly grows logarithmically with slip displacement x, as indicated by the dashed curves in the spectrograms in Figs 5 and S2 in supplementary material. H_G can also be calculated from the wear debris curves (V_{WD}), representing the volume of gouge particles per unit length produced by shearing and abrasion of partially damaged granular material incorporated from the adjacent damage zones (cf. Figs 4 and S1 in supplementary material). The gouge thickness is obtained by dividing V_{WD} by the solid fraction of the gouge. Note that the wear debris curves at submelting temperatures also grow logarithmically with slip, as indicated by linear trends in the semi-log plots (*cf.* Figs 4 and S1 in supplementary material). The V_{WD} is in fact a proxy of the thickness of the gouge zone since the average solid fraction of the gouge zone varies little with slip distance.

The logarithmic trend for H_G is consistent with models based on field observations of fault roughness as a function of slip at different scales, which predict that wear rate is roughly proportional to $1/x$ (i.e. the derivative of a logarithmic function) (Brodsky *et al.* 2011). According to these authors, the gradual smoothing of the faults reduces the efficiency of surface wear as protrusions are sequentially removed. This mechanism is visible in our simulations, where asperities are progressively smoothed during shearing, particularly in the bottom damage zone (*cf.* animation file in supplementary material). By contrast, the smoothing of the fault surface is incompatible with a linear increase of gouge thickness with slip displacement (Scholz 1987), where new asperities are constantly generated through re-roughening of the surface. Alternatively, DEM shear tests at low strain rates (Guo & Morgan 2007) indicate that the rate of gouge thickening decreases exponentially during the early phase of sliding and becomes approximately constant for large shear displacements. Their simulation results suggest that for large slips, shear strain is accommodated mainly by grain rolling and sliding within a well-developed gouge zone. As a result, the irregular fault surfaces are protected from further wear. However, the distinction between very low steady-state wear rates and a logarithmic trend for large shear displacements is not straightforward and will require more numerical analysis.

The values of gouge thickness as a function of slip displacement $H_G(x)$ are in good agreement with datasets for small-size faults in different rock types, which reveal a general positive correlation between fault core thickness and displacement/throw (Sperrevik *et al.* 2002; Choi *et al.* 2016). Moreover, the shape of curves $H_G(x)$ for phase 2 (i.e. in steady-state conditions at submelting temperature) is consistent with power-law relations suggested by conceptual models for the evolutionary processes of faults based on empirical relations (Torabi & Berg 2011). From the numerical side, our results are consistent with granular models showing shear-band localization zones with thicknesses between 10–20 particle diameters in shear tests performed under similar conditions to those in our simulations (Guo & Morgan 2007). Namely, the surface friction coefficient $\mu_s = 0.5$, the granular flow is quasi-static (i.e. the inertial number is low $I < 10^{-3}$), the shear loading is rate controlled, and friction and dilatancy have reached steady-state values.

4.3 Wear rate

To illustrate the evolution of wear rate as a function of lithostatic pressure, we selected the same two case studies as for the breakdown energy analysis at intermediate and high confining pressures ($\sigma_n' =$ 56.3 and 112.5 MPa, respectively) (runs 1a and 1c, Table 1). The slip velocity and weakening temperature are the same for both case studies ($V_S = 0.5$ m s^{-1} and $T_w = 500$ °C).

The wear rate in the damage zones WR ($= \partial V_{WD}/\partial x$) fluctuates with slip displacement and frictional strength, showing significant variations over two transient stages (cf. Fig. 7). During rupture initiation (phases 1 and 2), WR decays by one to two orders of magnitude, from ∼ $10^5 \mu$m m^{-1} to values between ∼ 10^3 and ∼ $10^4 \mu$m m^{-1} for intermediate and high confining pressures, respectively (indexes

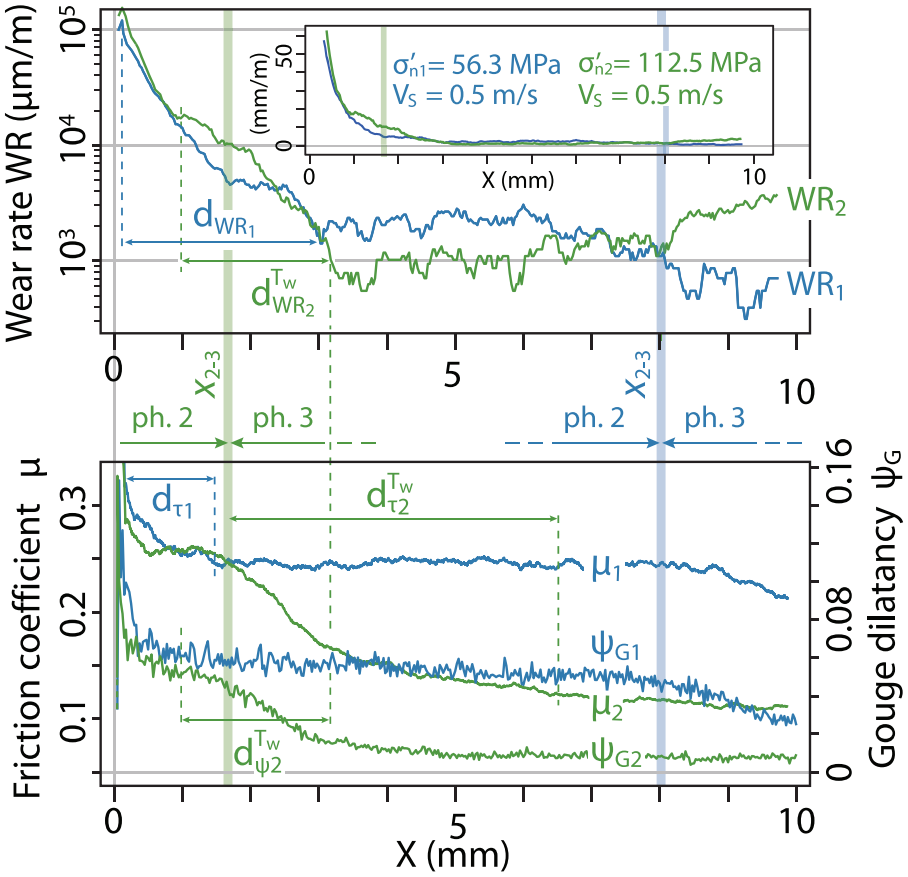

Figure 7. Wear rate, friction coefficient, and gouge dilatancy curves as a function of slip displacement for intermediate and high confining pressures (runs 1a and 1c, Table 1). Intermediate and high confining pressures are labeled with indexes 1 and 2, respectively. d_{WR1}, $d_{\tau 1}$: Critical decay distances for wear rate and shear stress at intermediate confining pressure and submelting temperatures, respectively. d^{Tw}_{WR2}, $d^{Tw}_{\tau 2}$, $d^{Tw}_{\Psi 2}$: Critical decay distances for wear rate, shear stress, and gouge dilatancy at high confining pressure and flash-heating temperatures, respectively. The onset of thermal weakening (i.e. phase 3) is indicated by vertical color stripes at slip distance x_{2-3}.

1 and 2 refer to intermediate and high confining pressures, respectively). Extreme values for *WR* result from crushing and fragmentation of cohesive clusters detached during the initial rupture (Togo & Shimamoto 2012). Note that the critical distance for wear rate decay is much longer than the corresponding distance for frictional decay at submelting temperatures (e.g. $d_{WR1} \gg d_{\tau 1}$, Fig. 7). In other words, the abrasion rate is still evolving even if the shear zone has reached a steady-state condition for friction and dilatancy. This feature is well illustrated for the intermediate confining pressure case study (blue curves, Fig. 7). It is also observed in high-velocity shear tests performed on carbonate samples at lower confining pressures (Boneh *et al.* 2013).

Steady-state and transient wear rates at submelting temperatures in our simulations increase with confining pressure and are poorly dependent on slip velocity. This behavior is consistent with results in the above-cited study for low-velocity experiments at low confining pressures (<6 MPa) and predicted by theoretical models (Lyakhovsky *et al.* 2014). This similarity is possibly due to a brittle deformation regime in the gouge, where thermal effects are not dominant. Moreover, the relative contribution of effective cohesion to the shear strength decreases significantly at high confining pressure (Estrada & Taboada 2013). Thus, for increasing confining pressure, the particle model tends to behave as a cohesionless frictional material, in which the average shear strain is distributed within a thicker gouge zone to reduce the inertial number and the shear strength (Parez *et al.* 2021).

The wear-rate decay during the initial transient stage is concomitant with a substantial decay in the shear-strain rate in the newly formed gouge. Shear strain rate decreases from $\sim 2 \times 10^5$ s^{-1} right after the frictional peak to $\sim 2 \times 10^4$ s^{-1} before thermal weakening. The wear- and shear-strain-rate simulation values are roughly one order of magnitude larger than those observed in high-velocity shear tests on granite and dolomite rock samples deformed at intermediate confining pressures (up to 30 MPa) (Chang *et al.* 2012). Initial wear rates in these earthquake-like laboratory experiments vary between 10^2 s^{-1} and 10^4 s^{-1} for strain rates of $\sim 10^4$ s^{-1}. Despite the difference in the magnitude for these parameters, the ratio of wear rate to strain rate is comparable in experimental tests and numerical models, suggesting a scaling law relating wear rate and shear strain rate during transient behavior.

The rapid decay of the wear rate at flash heating temperatures is correlated with the fall in the local friction coefficient of particles located in the core of the gouge zone (*cf.* Figs 5 and 7). Spectrograms show that the temperature gradient within the gouge layer is very high at the beginning of phase 3 (i.e. for slip displacement x_{2-3}). Thus, the sliding friction μ_s of particles in the gouge core drops to zero as they reach the weakening threshold. Conversely, particles adjacent to the damage zones are at much lower temperatures and

preserve their initial frictional strength ($\mu_s = 0.5$). At this stage, the gouge layer's frictional strength and shear strain are heterogeneous. Notably, shear strain tends to concentrate in the weaker central zone of the gouge layer, reducing shear strain and abrasion in the damage zone.

The transient regime for wear rate and gouge dilatancy at flash heating temperatures precedes the transient regime for frictional strength (cf. Figs 4 and 7). More precisely, the critical decay distances for wear rate and dilatancy (d_{WR2}^{Tw} and $d_{\Psi 2}^{Tw}$) are much shorter and shifted leftward relative to the critical decay distance for shear stress ($d_{\tau 2}^{Tw}$). The leftward shift suggests that frictionless particles begin to compact from the gouge core toward the damage zones as they have no dilatancy (Peyneau & Roux 2008; Azéma *et al.* 2015), localizing shear strain in the core and reducing the wear rate in the damage zones. Note that wear rate and gouge dilatancy reach the steady state well before frictional strength.

The asymmetrical shape of sigmoidal decreasing curves for friction in thermally weakened gouge is linked to the decrease in frictional heat dissipation as sliding friction tends to zero. Note that minimum frictional strength is reached for substantial slip displacements when all the gouge particles are at temperatures well above T_w. The decay of wear rate at flash heating temperatures is consistent with the model for fault weakening proposed by Reches & Lockner (2010) based on high-velocity shear tests of granite blocks. The model suggests that wear rate and frictional strength decrease concomitantly when increasing slip rates reach intermediate values ($V_S = 0.01-0.05$ m s^{-1}). However, the weakening mechanism is linked to powder lubrication and not to flash heating.

4.4 Energy budget of the shear zone

The breakdown energies consumed to generate the gouge and damage zones from cohesive granular material are compared with the energy consumed in on- and off-fault damage during dynamic (earthquake) rupture and slip (e.g. Johnson *et al.* 2021, and references therein). For this purpose, we calculate the breakdown energy components as a function of slip displacement, represented by cumulative curves and shaded areas in the (x, τ) plane (cf. Fig. 8). We also compare our results to fracture energy estimations for shear tests on rock samples (e.g. Nielsen *et al.* 2016a), which are based on the definition commonly used in seismology (*cf.* eq. 5). Note that fracture energy in seismology is often assimilated with the breakdown energy, as it includes all the energies due to plastic yielding and cracking (near fault tips and off-fault) (e.g. Kanamori & Rivera 2006; Chang *et al.* 2012).

The breakdown energy of the damage zones W_D shows a complex fluctuating pattern around zero, which has been suggested for the total breakdown energy in conceptual models (Tinti *et al.* 2005; Johnson *et al.* 2021). More precisely, we observe long-period damped fluctuations (cf. Fig. 8, bottom), which contrast with the widespread supposition that W_D is an increasing function of slip (Torabi & Berg 2011; Soliva *et al.* 2013). Negative energy values primarily result from a decrease in the damage zone's thickness and dilatancy during the shear zone growth phase (e.g. phase 2). In addition, note that peak and through values in W_D follow corresponding shear-stress fluctuations around average values, suggesting that the two wave forms are correlated (blue and green curves represent exponential approximations for τ, Fig. 8, bottom). These fluctuations, however, may be linked to the velocity step function applied on our shear tests, which induces a much greater slip acceleration than those for earthquakes (3–6.5 m/s^2) (Nielsen *et al.* 2016a). Nevertheless, the slope of the velocity step has little impact on the evolution of the shear zone in phases 2 and 3 (*cf.* Figs S6 and S7, supplementary material). On the other hand, the breakdown energy components of the gouge zone W_G (yellow, pink, and light-blue areas) follow a similar decaying trend as the average fracture energy in phase 2 (the gray area bounded by the average shear τ and the steady-state shear stress τ_{SS}, Fig. 8). However, W_G represents a varying proportion of the fracture energy as a function of slip displacement. Thus, no simple correlation can be established between fracture energy and the breakdown energy components as a function of slip displacement.

The breakdown energy in our experimental setting is fundamentally different from the fracture energy determined from rock mechanics tests and kinematic slip models for earthquakes (*cf.* Section 3.2) (Kanamori & Rivera 2006; Kammer & McLaskey 2019; Ke *et al.* 2022). However, fracture energy is commonly used as a proxy for breakdown energy during earthquake rupture in theoretical, experimental, and geological studies (e.g. Niemeijer *et al.* 2012; Togo & Shimamoto 2012; Passelègue *et al.* 2016a). The amalgam between these two terms is due to deep uncertainty regarding the on- and off-fault fracturing and dilatancy during dynamic rupture (Johnson *et al.* 2021).

The fracture energies at submelting and flash heating temperatures in our simulations ($\Gamma^{p2} \sim 3$ kJ m^{-2} and $\Gamma^{p3} \sim 50$ kJ m^{-2}) are slightly higher than those estimated for comparable slips ($\sim$ 0.5–1.5 and $\sim$ 10 mm, respectively) in high-velocity friction experiments on gouge and bare rock and in small earthquakes (e.g. Nielsen *et al.* 2016b,and references therein). This difference is not surprising since several rheological and geometrical dissimilarities exist between the granular model and experimental tests or natural faults, which may increase or decrease fracture energy. For example, particles in the granular model cannot fragment, increasing the strength peak, dilatancy values, and fracture energies, especially in 2-D models. Conversely, the macroscopic frictional strength of granular samples composed of disks is lower than those for most rocks generally composed of angular grains, reducing fracture energy (Taboada *et al.* 2006). Likewise, the flash heating temperature in the two case studies (500° C) is lower than for most rock minerals, reducing the distance for flash-heating initiation and fracture energy Γ^{p3}. These properties can be introduced in DEM models to satisfy better the similarity criteria for dynamic rupture in natural conditions.

Our results suggest that dilatancy is the primary energy sink within the damage zones for dynamic shearing at intermediate and high confining pressures. In contrast, decohesion and dilatancy are the major energy sinks linked to gouge formation at intermediate pressures, whereas dilatancy and debonding frictional energies predominate at high confining pressures. The prevalence of dilatancy energy may be due to the absence of fragmentation of micrometric-scale particles in our model, which increases surface energy and dilatancy (Nguyen & Einav 2009; Johnson *et al.* 2021). However, our average size particle (10 μm) is taken as the lower limit of the dynamic fragment size of mineral grains (e.g. garnets) for surface energy calculations resulting from coseismic damage (Johnson *et al.* 2021).

Notwithstanding the dissimilarities between the granular model and dynamic rupture in earthquake faults, our Mohr-Coulomb contact-strength law and the resulting decomposition of breakdown energy (i.e. into decohesion and debonding frictional components) are consistent with deformation mechanisms identified in numerical analogs for hard rocks sheared at similar confining pressures (50 MPa) (Vora & Morgan 2019). At this confining pressure, shear microcracks largely control fault growth and account for 90 per cent

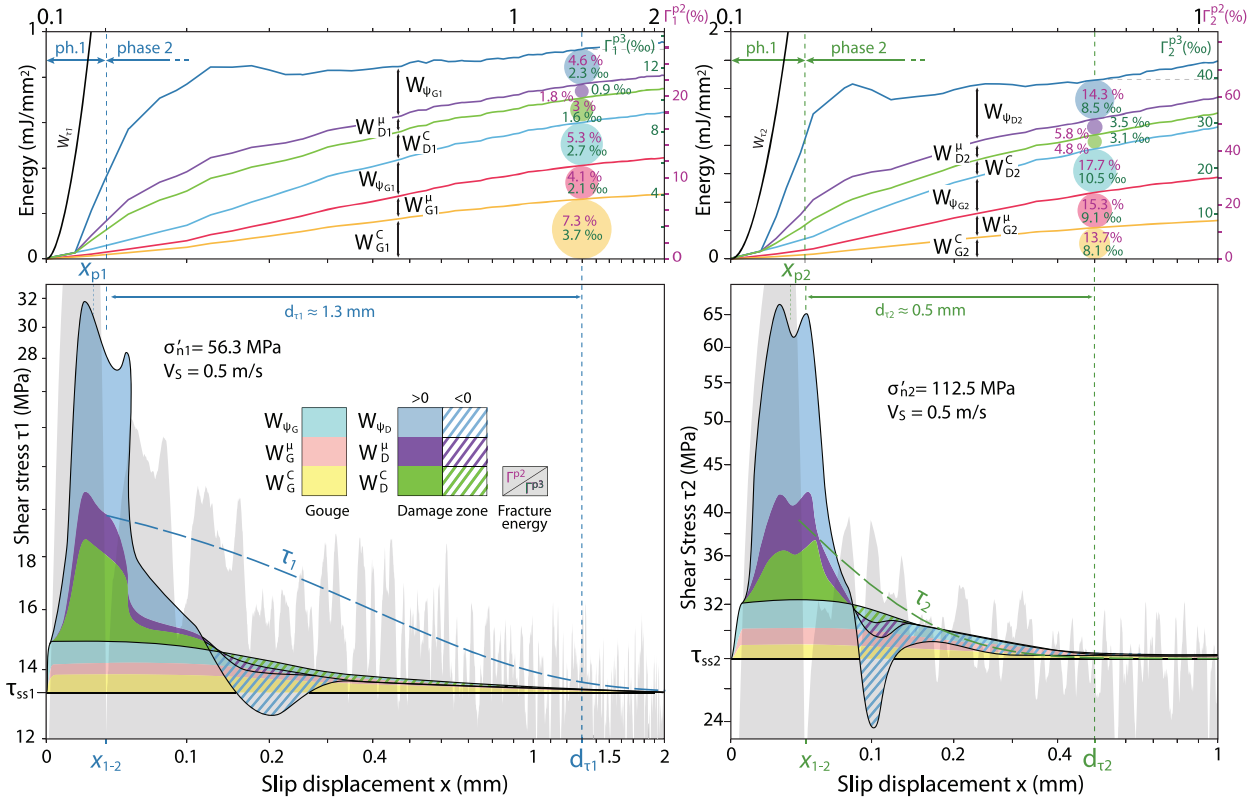

Figure 8. Breakdown energy components for the gouge and damage zones as a function of slip displacement during rupture initiation represented by cumulative curves and shaded areas in the (x, τ) plane (runs 1a and 1c, Table 1). Intermediate and high confining pressures are labeled with indexes 1 and 2 (left and right plots), respectively. Dashed curves are exponential approximations of the shear stress. d_τ: Critical decay distance for shear stress. W_G^C, W_G^μ, W_{Ψ_G}: Decohesion energy, debonding frictional energy, and dilatancy energy for the gouge zone (yellow, pink, and light blue colors, respectively). W_D^C, W_D^μ, W_{Ψ_D}: Decohesion energy, debonding frictional energy, and dilatancy energy for the damage zones (green, purple, and blue colors, respectively). Colored hatchings represent negative energy values for W_D. The magnitude of energy components is given by the relative size of the corresponding colored circles (top). Γ^{p2}, Γ^{p3}: Fracture energies at the end of transient regimes in phases 2 and 3, respectively (i.e. relative to brittle and thermally weakened steady states) (grey shading, bottom). Fracture energy values are defined inside colored circles according to the pink and green scales.

of the breakdown energy. However, the dilatancy energy component and the strain rate in these tests are much lower than in our simulations.

The breakdown energies determined in our study cases (∼1–2 kJ m^{-2}, Fig. 8, top) are similar to those predicted from numerical simulations and seismological studies for millimeter-scale slips (Abercrombie & Rice 2005; Ke *et al.* 2022). Contrastingly, the geological estimates for the breakdown energies are several orders of magnitude higher than our results since they generally correspond to seismic events with higher coseismic slips (Chester *et al.* 2005; Reches & Dewers 2005; Tinti *et al.* 2005; Pittarello *et al.* 2008; Johnson *et al.* 2021). The surface energy consumed in fragmentation during coseismic deformation can be as low as ∼40 kJ m^{-2} (Olgaard & Brace 1983; Johnson *et al.* 2021), which is still one order of magnitude larger than our estimates. In this study, the shear zone formed during an earthquake of magnitude 2.1 at 2 km depth, with average offset 50–60 mm, average thickness 10–50 mm, and average driving stress 40–70 MPa (similar to our intermediate confining pressure case study). The gouge particles result from crushing and fragmentation of unaltered quartzites, with sizes ranging from the original grain size (0.5 mm) to less than 0.05 μm (small particles are highly angular whereas large particles are slightly subrounded). The higher breakdown energy observed in this study is presumably linked with particle angularity (which increases frictional strength), intense fragmentation of quartz grains within a thicker gouge layer, and higher slip displacements.

5 CONCLUSION

This paper deals with the spatio-temporal evolution of a seismic shear zone as a function of confining pressure, slip velocity, and flash-heating temperature, from a discrete element perspective. Shear localization along a pre-existing fracture is triggered by a velocity step function imposed on the bottom wall of a wrap-around granular sample composed of micrometric bonded disks. Shear-zone growth is associated with progressive abrasion of granular material in the damage zones surrounding the gouge zone. According to parametric studies, the mechanical behavior of the shear zone exhibits three distinct phases.

In the initial phase of rupture propagation, friction and dilatancy curves are approximated by left skew (asymmetric) peak functions. The amplitude and geometry of peaks are controlled primarily by confining pressure (and not by slip velocity). For intermediate confining pressures, the asperities on the two mating shear surfaces tend to surmount each other, whereas they tend to be sheared off for high confinements.

In the intermediate phase of shear-zone growth, the model displays an initial transient stage that evolves toward a specific steady

state at submelting temperatures (phase 2). Average friction, dilatancy, and wear rate asymptotically approach steady values. The thickening of the gouge zone with slip displacement follows a logarithmic trend, in agreement with the volume of wear debris abraded from the surrounding damage zones. According to the inertial number, seismic shearing occurs under a quasi-static strain regime in which dynamic effects are not significant, despite high seismic shear rates. This result is ascribable to high confining pressures and small particle sizes considered in the models. Furthermore, it explains the constancy of steady-state friction and dilatancy observed in all simulations regardless of slip velocity, confining pressure, and gouge zone thickness.

In the final phase of shear weakening, the model evolves toward a new steady state at flash-heating temperatures (phase 3). Average friction can be approximated by an asymmetrical sigmoidal decreasing curve that asymptotically approaches steady-state values lower than for phase 2. Predictably, the thermally weakened friction in the steady state (μ_{ss} ~0.1) is close to the frictional strength of frictionless granular samples sheared in quasi-static conditions, in line with the null contact friction coefficient defined for particles above the flash heating temperature. Silt-sized frictionless particles in the gouge zone behave as a thin deforming layer of powder lubricant that reduces frictional strength during earthquake instabilities (Reches & Lockner 2010).

The breakdown energy consumed to generate the gouge and damage zones during rupture initiation fundamentally differs from the fracture energy determined in rock and earthquake mechanics, which is based on the post-failure integral of the dynamic weakening curve (eq. 5). The breakdown energy of the damage zones shows long-period damped oscillations weakly correlated with shear-stress fluctuations around average decaying values. Our results suggest that dilatancy is the primary energy sink within the damage zones in steady state. The breakdown energy components of the gouge zone follow a similar decaying trend as the average fracture energy but over a longer critical distance. Decohesion and dilatancy are the major energy sinks linked to gouge formation at intermediate pressures. In contrast, dilatancy and debonding frictional energies predominate at high confining pressures. Breakdown energy is equivalent to a fraction of fracture energy which nearly triples when doubling the confining pressure.

Discrete element modeling offers unique and fundamental insights into the complex micro-mechanical processes involved in seismic shearing. However, further work is required to improve the similarity between the rheologies of the granular material and the seismic shear zone. The shear strength scaling at submelting temperatures for disks assemblies can be achieved by introducing a rolling friction coefficient μ_R identified as a shape parameter representing particle angularity while using circular particles (Estrada *et al.* 2011). This parameter defines a threshold value for transmitting contact torques between disks, increasing the frictional strength to more representative values of rock materials. The polymineralic character of rocks can be introduced by defining strength parameters according to a specific grain typology (i.e. sliding friction coefficient, cohesion, and flash heating temperature). Introducing particle fragmentation is also essential as it contributes significantly to the breakdown energy. Fragmentation can be simulated by generating particle clusters with specific bonding laws representative of mineral strength. Besides, formulating a thermal model that enables the refinement of the temperature distribution at particle scale (e.g. in the vicinity of contacts and the core) will improve the precision of the thermo-mechanical evolution of the shear zone.

Granular models are also a valuable tool for examining the mechanical behavior of a seismic fault for a specific earthquake by setting boundary conditions according to source-time functions, which prescribe the slip-velocity evolution during rupture propagation (Tinti 2005; Noda & Lapusta 2013). The detailed mechanical analysis of a small shear zone section during coseismic slip is essential for unraveling how a fault's strength evolves with slip or slip rate and how much energy is dissipated or available for continued rupture. A future challenge is implementing discrete element models in 3-D that simultaneously consider flash heating of asperity contacts and thermal pressurization of the pore fluids. Moreover, such simulations will require lengthy processing times (much longer than 2-D models) as the number of particles will increase by two orders of magnitude.

ACKNOWLEDGMENTS

The authors are grateful to Jean-Noël Roux for fruitful discussions and to the Editor and three anonymous reviewers for detailed comments, which improved the manuscript considerably. This study was sponsored by the ALEAS program (a join CNRS-INSU grant) and by the Montpellier University Support of Research project. The authors wish to thank the developers of the LMGC90 platform who have allowed this investigation. We acknowledge the support of the High-Performance Computing Platform MESOLR. We thank Anne Delplanque for her technical help.

REFERENCES

Abercrombie, R.E. & Rice, J.R., 2005. Can observations of earthquake scaling constrain slip weakening?, *Geophys. J. Int.,* **162**(2), 406–424.

Passelègue, F.X., Schubnel, A. & Violay, M., 2018. Dynamic weakening during earthquakes controlled by fluid thermodynamics, *Nat. Commun.,* **9,** 3074.10.1038/s41467-018-05603-9

Aharonov, E. & Scholz, C.H., 2018. A physics-based rock friction constitutive law: steady state friction: a physics-based friction law, *J. Geophys. Res.,* **123**(2), 1591–1614.10.1002/2016JB013829

Alonso-Marroquín, F., Vardoulakis, I., Herrmann, H.J., Weatherley, D. & Mora, P., 2006. Effect of rolling on dissipation in fault gouges, *Phys. Rev. E,* **74,** 031306.

An, L.-J. & Sammis, C.G., 1994. Particle size distribution of cataclastic fault materials from Southern California: A 3-D study, *Pure Appl. Geophys.,* **143**(1-3), 203–227.

Andrews, D.J., 2005. Rupture dynamics with energy loss outside the slip zone, *J. Geophys. Res.,* **110**(B1), B01307.

Azéma, E., Radjaï, F. & Roux, J.-N., 2015. Internal friction and absence of dilatancy of packings of frictionless polygons, *Phys. Rev. E,* **91,** 010202.

Barbery, M.R., Chester, F.M. & Chester, J.S., 2021. Characterizing the distribution of temperature and normal stress on flash heated granite surfaces at seismic slip rates, *J. Geophys. Res.,* **126**(5), e2020JB021353.

Barton, N., 2013. Shear strength criteria for rock, rock joints, rockfill and rock masses: problems and some solutions, *J. Rock Mech. Geotech. Eng.,* **5**(4), 249–261.

Baumberger, T. & Caroli, C., 2006. Solid friction from stick–slip down to pinning and aging, *Adv. Phys.,* **55**(3–4), 279–348.

Beeler, N.M., 2006. *Inferring Earthquake Source Properties from Laboratory Observations and the Scope of Lab Contributions to Source Physics,* pp. 99–119, American Geophysical Union (AGU).

Beeler, N.M., Tullis, T.E. & Goldsby, D.L., 2008. Constitutive relationships and physical basis of fault strength due to flash heating, *J. Geophys. Res.,* **113**(B1), B01401.

Ben-David, O. & Fineberg, J., 2011. Static friction coefficient is not a material constant, *Phys. Rev. Lett.,* **106,** 254301.

Berthier, Y., Vincent, V. & Godet, M., 1988. Velocity accommodation in fretting, *Wear,* **125**(1), 25–38.

Bestmann, M., Pennacchioni, G., Nielsen, S., Göken, M. & de Wall, H., 2012. Deformation and ultra fine dynamic recrystallization of quartz in pseudotachylyte-bearing brittle faults: A matter of a few seconds, *J. Struct. Geol.,* **38,** 21–38.

Boneh, Y., Sagy, A. & Reches, Z., 2013. Frictional strength and wear-rate of carbonate faults during high-velocity, steady-state sliding, *Earth Planet. Sci. Lett.,* **381,** 127–137.

Boullier, A.-M., Yeh, E.-C., Boutareaud, S., Song, S.-R. & Tsai, C.-H., 2009. Microscale anatomy of the 1999 Chi-Chi earthquake fault zone, *Geochem. Geophys. Geosyst.,* **10**(3), 1–25.

Bowden, F.P. & Tabor, D., 1964. *Friction and Lubrication of Solids, Part II,* Oxford University Press.

Brantut, N. & Platt, J.D., 2017. *Dynamic Weakening and the Depth Dependence of Earthquake Faulting,* chap. 9, pp. 171–194, American Geophysical Union (AGU).

Brantut, N. & Viesca, R.C., 2017. The fracture energy of ruptures driven by flash heating, *Geophys. Res. Lett.,* **44**(13), 6718–6725.

Brodsky, E., Gilchrist, J., Sagy, A. & Collettini, C., 2011. Faults smooth gradually as a function of slip, *Earth Planet. Sci. Lett.,* **302**(1), 185–193.

Brodsky, E.E., Kirkpatrick, J.D. & Candela, T., 2016. Constraints from fault roughness on the scale-dependent strength of rocks, *Geology,* **44**(1), 19–22.

Burov, E.B., 2011. Rheology and strength of the lithosphere, *Mar. Petrol. Geol.,* **28**(8), 1402–1443.

Cermak, V. & Rybach, L., 1982. *Thermal Properties: Thermal Conductivity and Specific Heat of Minerals and Rocks,* Vol. **1a,** pp. 305–343, Springer Verlag.

Champagne, M., Renouf, M. & Berthier, Y., 2014. Modeling wear for heterogeneous bi-phasic materials using discrete elements approach, *ASME J. Tribol.,* **136**(2), 021603.

Chang, J.C., Lockner, D.A. & Reches, Z., 2012. Rapid acceleration leads to rapid weakening in earthquake-like laboratory experiments, *Science,* **338**(6103), 101–105.

Chen, X., Morgan, C.B., Carpenter, B.M. & Reches, Z., 2019. Weakening mechanisms of alpine fault gouge in high-velocity shear experiments, *J. Geophys. Res.,* **124**(7), 7413–7428.

Chester, J., Chester, F. & Kronenberg, A., 2005. Fracture surface energy of the punchbowl fault, San Andreas system, *Nature,* **437,** 133–136.

Chester, J.S. & Goldsby, D.L., 2003. *Microscale characterization of natural and experimental slip surfaces relevant to earthquake mechanics,* Tech. rep., SCEC Annual Report. https://files.scec.org/s3fs-public/reports/2003/02052_report.pdf

Choi, J.-H., Edwards, P., Ko, K. & Kim, Y.-S., 2016. Definition and classification of fault damage zones: a review and a new methodological approach, *Ear. Sci. Rev.,* **152,** 70–87.

Christov, I.C. & Stone, H.A., 2014. Shear dispersion in dense granular flows, *Gran. Matt.,* **16**(4), 509–515.

Collettini, C., Viti, C., Tesei, T. & Mollo, S., 2013. Thermal decomposition along natural carbonate faults during earthquakes, *Geology,* **41**(8), 927–930.

Cooper, M.G., Mikic, B.B. & Yovanovich, M.M., 1969. Thermal contact conductance, *Int. J. Heat Mass Tran.,* **12,** 279–300.

Di Toro, G., Goldsby, D. & Tullis, T., 2004. Friction falls towards zero in quartz rock as slip velocity approaches seismic rates, *Nature,* **427,** 436–439.

Di Toro, G., Hirose, T., Nielsen, S., Pennacchioni, G. & Shimamoto, T., 2006. Natural and experimental evidence of melt lubrication of faults during earthquakes, *Science,* **311**(5761), 647–649.

Di Toro, G. *et al.*, 2011. Fault lubrication during earthquakes, *Nature,* **471**(7339), 494–498.

Dieterich, J., 1978. Time-dependent friction and the mechanics of stick-slip, *PAGEOPH,* **116,** 790–806.

Dieterich, J.H. & Kilgore, B.D., 1994. Direct observation of frictional contacts: New insights for state-dependent properties, *PAGEOPH,* **143,** 283–302.

Dieterich, J.H. & Kilgore, B.D., 1996. Imaging surface contacts: power law contact distributions and contact stresses in quartz, calcite, glass and acrylic plastic, *Tectonophysics,* **256**(1–4), 219–239.

Estrada, N. & Taboada, A., 2013. Yield surfaces and plastic potentials of cemented granular materials from discrete element simulations, *Comput. Geotech.,* **49,** 62–69.

Estrada, N., Taboada, A. & Radjaï, F., 2008. Shear strength and force transmission in granular media with rolling resistance, *Phys. Rev. E,* **78,** 021301.

Estrada, N., Azéma, E., Radjai, F. & Taboada, A., 2011. Identification of rolling resistance as a shape parameter in sheared granular media, *Phys. Rev. E,* **84**(1), 011306.

Faulkner, D.R., Sanchez-Roa, C., Boulton, C. & den Hartog, S. A.M., 2018. Pore fluid pressure development in compacting fault Gouge in theory, experiments, and nature, *J. Geophys. Res.,* **123**(1), 226–241.

Forgber, T. & Radl, S., 2018. A novel approach to calculate radiative thermal exchange in coupled particle simulations, *Powder Technol.,* **323,** 24–44.

Frye, K.M. & Marone, C., 2002. The effect of particle dimensionality on granular friction in laboratory shear zones, *Geophys. Res. Lett.,* **29**(19), 22–1-22-4.

GDR MiDi, 2004. On dense granular flows, *Eur. Phys. J. E,* **14**(4), 341–365.

Goldsby, D.L. & Tullis, T.E., 2002. Low frictional strength of quartz rocks at subseismic slip rates, *Geophys. Res. Lett.,* **29**(17), 1844.

Goldsby, D.L. & Tullis, T.E., 2011. Flash heating leads to low frictional strength of crustal rocks at earthquake slip rates, *Science,* **334**(6053), 216–218.

Greenwood, J.A. & Williamson, J. B.P., 1966. The contact of nominally flat rough surfaces, *Proc. Roy. Soc. A,* **495,** 300–319.

Guo, Y. & Morgan, J.K., 2007. Fault gouge evolution and its dependence on normal stress and rock strength – results of discrete element simulations: gouge zone properties, *J. Geophys. Res.,* **112,** B10403.

Guo, Y. & Morgan, J.K., 2008. Fault gouge evolution and its dependence on normal stress and rock strength–results of discrete element simulations: gouge zone micromechanics, *J. Geophys. Res.,* **113,** B08417.

Hackston, A. & Rutter, E., 2016. The Mohr-Coulomb criterion for intact rock strength and friction – a re-evaluation and consideration of failure under polyaxial stresses, *Solid Earth,* **7**(2), 493–508.

Han, R., Hirose, T., Jeong, G.Y., Ando, J.-I. & Mukoyoshi, H., 2014. Frictional melting of clayey gouge during seismic fault slip: Experimental observation and implications, *Geophys. Res. Lett.,* **41**(15), 5457–5466.

Hirose, T. & Shimamoto, T., 2003. Fractal dimension of molten surfaces as a possible parameter to infer the slip-weakening distance of faults from natural pseudotachylytes, *J. Struct. Geol.,* **25**(10), 1569–1574.

Hirose, T. & Shimamoto, T., 2005. Growth of molten zone as a mechanism of slip weakening of simulated faults in Gabbro during frictional melting, *J. Geophys. Res.,* **110,** B05202.

Hoek, E. & Martin, C.D., 2014. Fracture initiation and propagation in intact rock – a review, *J. Rock Mech. Geotech. Eng.,* **6**(4), 287–300.

Jean, M., 1999. The non-smooth contact dynamics method, *Comput. Methods Appl. Mech. Eng.,* **177**(3–4), 235–257.

Johnson, S.E., Song, W.J., Vel, S.S., Song, B.R. & Gerbi, C.C., 2021. Energy partitioning, dynamic fragmentation, and off-fault damage in the earthquake source volume, *J. Geophys. Res.,* **126**(11), e2021JB022616.

Bradbury, K.K., Evans, J.P., Chester, J.S., Chester, F.M. & Kirschner, D.L., 2011. Lithology and internal structure of the san andreas fault at depth based on characterization of phase 3 whole-rock core in the san andreas fault observatory at depth (safod) borehole, *Earth Planet. Sci. Lett.,* **310**(1), 131–144.

Kammer, D.S. & McLaskey, G.C., 2019. Fracture energy estimates from large-scale laboratory earthquakes, *Earth Planet. Sci. Lett.,* **511,** 36–43.

Kanamori, H. & Rivera, L., 2006. Energy partitioning during an earthquake, *Geophysical Monograph Series,* Vol. **170,** pp. 3–13, eds Abercrombie, R., McGarr, A., Kanamori, H. & Di Toro, G., American Geophysical Union, Washington, D.C.

Ke, C.-Y., McLaskey, G.C. & Kammer, D.S., 2022. Earthquake breakdown energy scaling despite constant fracture energy, *Nat. Commun.,* **13,** 1005.

Kennedy, F.E., 1981. Surface temperature in sliding systems - a finite element analysis, *J. Lubr. Technol.,* **103,** 90–96.

Kirkpatrick, J.D., Rowe, C.D., White, J.C. & Brodsky, E.E., 2013. Silica gel formation during fault slip: Evidence from the rock record, *Geology,* **41**(9), 1015–1018.

Koval, G., Roux, J.-N., Corfdir, A. & Chevoir, F., 2009. Annular shear of cohesionless granular materials: from the inertial to quasistatic regime, *Phys. Rev. E,* **79**(2), 021306.

Kudryavtsev, Y.V., Gelinck, E. & Fischer, H.R., 2009. Theoretical investigation of van der Waals forces between solid surfaces at nanoscales, *Surf. Sci.,* **603,** 2580–2587.

Kuo, L.-W., Y.-F. S., Yang, C.-M., Song, S.-R., Wang, C.-C., Dong, J.-J., Suppe, J. & Shimamoto, T., 2015. Ultrafine spherical quartz formation during seismic fault slip: Natural and experimental evidence and its implications, *Tectonophysics,* **664,** 98–108.

Lachenbruch, A.H. & Sass, J.H., 1980. Heat flow and energetics of the san andreas fault zone, *J. Geophys. Res.,* **85**(B11), 6185–6222.

Laraqi, N. & Bairi, A., 2002. Theory of thermal resistance between solids with randomly sized and located contacts, *Int. J. Heat Mass Tran.,* **45**(20), 4175–4180.

Lockner, D.A., Kilgore, B.D., Beeler, N.M. & Moore, D.E., 2017. The transition from frictional sliding to shear melting in laboratory stick-slip experiments, *Geophysical Monograph Series,* pp. 103–131, eds Thomas, M.Y., Mitchell, T.M. & Bhat, H.S., John Wiley & Sons, Inc., Hoboken, NJ, USA.

Lyakhovsky, V., Sagy, A., Boneh, Y. & Reches, Z., 2014. Fault wear by damage evolution during steady-state slip, *Pure Appl. Geophys.,* **171,** 3143–3157.

Makedonska, N., Sparks, D.W., Aharonov, E. & Goren, L., 2011. Friction versus dilation revisited: Insights from theoretical and numerical models, *J. Geophys. Res.,* **116**(B9), B09302.

Marone, C., 1998. Laboratory-derived friction laws and their application to seismic faulting, *Annu. Rev. Earth Pl. Sc.,* **26**(1), 643–696.

McLaskey, G.C., Thomas, A.M., Glaser, S.D. & Nadeau, R.M., 2012. Fault healing promotes high-frequency earthquakes in laboratory experiments and on natural faults, *Nature,* **491**(7422), 101–104.

Mitchell, E.K., Fialko, Y. & Brown, K.M., 2013. Temperature dependence of frictional healing of westerly granite: experimental observations and numerical simulations, *Geochem. Geophys. Geosys.,* **14**(3), 567–582.

Mollon, G., Aubry, J. & Schubnel, A., 2021. Simulating melting in 2D seismic fault gouge, *J. Geophys. Res.,* **126**(6).

Moreau, J.J., 1988. Unilateral contact and dry friction in finite freedom dynamics, *Nonsmooth Mechanics and Applications,* pp. 1–82, eds Moreau, J.J. & Panagiotopoulos, P.D., Springer Vienna, Vienna.

Nakatani, M. & Scholz, C.H., 2006. Intrinsic and apparent short-time limits for fault healing: theory, observations, and implications for velocity-dependent friction, *J. Geophys. Res.,* **111,** B12208.

Nguyen, G.D. & Einav, I., 2009. The energetics of cataclasis based on breakage mechanics, *Pure Appl. Geophys.,* **166**(10–11), 1693–1724.

Nielsen, S., 2017. From slow to fast faulting: recent challenges in earthquake fault mechanics, *Phil. Trans. R. Soc. A.,* **375**(2103), 20160016.

Nielsen, S., Spagnuolo, E., Smith, S. A.F., Violay, M., Di Toro, G. & Bistacchi, A., 2016a. Scaling in natural and laboratory earthquakes, *Geophys. Res. Lett.,* **43**(4), 1504–1510.

Nielsen, S., Spagnuolo, E., Violay, M., Smith, S. A.F., Di Toro, G. & Bistacchi, A., 2016b. G: Fracture energy, friction and dissipation in earthquakes, *J. Seismol,* **20,** 1187–1205.

Nielsen, S., Spagnuolo, E., Violay, M. & Di Toro, G., 2021. Thermal weakening friction during seismic slip: experiments and models with heat sources and sinks, *J. Geophys. Res.,* **126**(5), e2020JB020652.

Niemeijer, A., Di Toro, G., Griffith, W.A., Bistacchi, A., Smith, S.A.F. & Nielsen, S., 2012. Inferring earthquake physics and chemistry using an integrated field and laboratory approach, *J. Struct. Geol.,* **39,** 2–36.

Noda, H., 2008. Frictional constitutive law at intermediate slip rates accounting for flash heating and thermally activated slip process, *J. Geophys. Res.,* **113,** B09302.

Noda, H. & Lapusta, N., 2013. Stable creeping fault segments can become destructive as a result of dynamic weakening, *Nature,* **493**(7433), 518–521.

Olgaard, D.L. & Brace, W.F., 1983. The microstructure of gouge from a mining-induced seismic shear zone, *Int. J. Rock Mech. Mining Sci. Geomech. Abstr.,* **20**(1), 11–19.

Parez, S., Travnickova, T., Svoboda, M. & Aharonov, E., 2021. Strain localization in planar shear of granular media: the role of porosity and boundary conditions, *Euro. Phys. J. E,* **44**(11).

Passelègue, F.X., Schubnel, A., Nielsen, S., Bhat, H.S., Deldicque, D. & Madariaga, R., 2016a. Dynamic rupture processes inferred from laboratory microearthquakes, *J. Geophys. Res.,* **121**(6), 4343–4365.

Passelègue, F.X., Spagnuolo, E., Violay, M., Nielsen, S., Di Toro, G. & Schubnel, A., 2016b. Frictional evolution, acoustic emissions activity, and off-fault damage in simulated faults sheared at seismic slip rates, *J. Geophys. Res.,* **121**(10), 7490–7513.

Persson, B. N.J., 2001. Theory of rubber friction and contact mechanics, *J. Chem. Phys.,* **115**(8), 3840–3861.

Peyneau, P.-E. & Roux, J.-N., 2008. Frictionless bead packs have macroscopic friction, but no dilatancy, *Phys. Rev. E,* **78**(1), 011307.

Pittarello, L., Di Toro, G., Bizzarri, A., Pennacchioni, G., Hadizadeh, J. & Cocco, M., 2008. Energy partitioning during seismic slip in pseudotachylyte-bearing faults (gole larghe fault, adamello, italy), *Earth Planet. Sci. Lett.,* **269**(1), 131–139.

Proctor, B.P., Mitchell, T.M., Hirth, G., Goldsby, D., Zorzi, F., Platt, J.D. & Di Toro, G., 2014. Dynamic weakening of serpentinite gouges and bare surfaces at seismic slip rates, *J. Geophys. Res.,* **119**(11), 8107–8131.

Radjai, F. & Dubois, F., 2011. *Discrete-Element Modeling of Granular Materials,* Wiley-Iste, ISBN: 978-1-848-21260-2.

Reches, Z. & Dewers, T.A., 2005. Gouge formation by dynamic pulverization during earthquake rupture, *Earth Planet. Sci. Lett.,* **235**(1), 361–374.

Reches, Z. & Lockner, D.A., 2010. Fault weakening and earthquake instability by powder lubrication, *Nature,* **467**(7314), 452–455.

Rempel, A.W. & Rice, J.R., 2006. Thermal pressurization and onset of melting in fault zones, *J. Geophys. Res.,* **111**(B9), B09314.

Rempel, A.W. & Weaver, S.L., 2008. A model for flash weakening by asperity melting during high-speed earthquake slip, *J. Geophys. Res.,* **113**(B11), B11308.

Renouf, M. & Berthier, Y., 2011. *Numerical Modeling of Heat Production and Transmission,* pp. 347–366, Wiley, Chap 13 in Discrete-element Modeling of Granular Materials ISBN : 9781848212602.

Renouf, M., Dubois, F. & Alart, P., 2004. A parallel version of the non smooth contact dynamics algorithm applied to the simulation of granular media, *J. Comput. Appl. Math.,* **168**(1–2), 375–382.

Rice, J.R., 2006. Heating and weakening of faults during earthquake slip, *J. Geophys. Res.,* **111**(B5), 1–29.

Rice, J.R., 2017. Heating, weakening and shear localization in earthquake rupture, *Phil. Trans. R. Soc. A.,* **375**(2103), 20160015.

Rice, J.R., Rudnicki, J.W. & Platt, J.D., 2014. Stability and localization of rapid shear in fluid-saturated fault gouge: 1. Linearized stability analysis, *J. Geophys. Res.,* **119**(5), 4311–4333.

Richard, D., Iordanoff, I., Renouf, M. & Berthier, Y., 2008. Thermal study of the dry sliding contact with third body presence, *ASME J. Tribol.,* **130**(3).

Riviere, J., Renouf, M. & Berthier, Y., 2015. Thermo-mechanical investigations of a tribological interface, *Tribol. Lett.,* **58,** 48.

Rognon, P. & Einav, I., 2010. Thermal transients and convective particle motion in dense granular materials, *Phys. Rev. Lett.,* **105,** 218301.

Rognon, P.G., Roux, J.-N., Wolf, D., Naaïm, M. & Chevoir, F., 2006. Rheophysics of cohesive granular materials, *Europhys. Lett.,* **74**(4), 644–650.

Rubinstein, S., Cohen, G. & Fineberg, J., 2004. Detachment fronts and the onset of dynamic friction, *Nature,* **430,** 1005–1009.

Ruina, A., 1983. Slip instability and state variable friction laws, *J. Geophys. Res.,* **88**(B12), 10359–10370.

Scholz, C.H., 1987. Wear and gouge formation in brittle faulting, *Geology,* **15,** 493–495.

Scholz, C.H., 1998. Earthquakes and friction laws, *Nature,* **391**(6662), 37–42.

Smeraglia, L. *et al.*, 2017. Microstructural evidence for seismic and aseismic slips along clay-bearing, carbonate faults, *J. Geophys. Res.,* **122**(5), 3895–3915.

Smith, S.A.F., Billi, A., Toro, G.D. & R.S., 2011. Principal slip zones in limestone: Microstructural characterization and implications for the seismic cycle (tre monti fault, central apennines, italy), *Pure Appl. Geophys.,* **168,** 2365–2393.

Soliva, R., Schultz, R.A., Ballas, G., Taboada, A., Wibberley, C., Saillet, E. & Benedicto, A., 2013. A model of strain localization in porous sandstone as a function of tectonic setting, burial and material properties; new insight from provence (southern france), *J. Struct. Geol.,* **49,** 50–63.

Spagnuolo, E., Plümper, O., Violay, M., Cavallo, A. & Di Toro, G., 2016. Dislocation motion and the microphysics of flash heating and weakening of faults during earthquakes, *Crystals,* **6**(7), 83.

Sperrevik, S., Gillespie, P.A., Fisher, Q.J., Halvorsen, T. & Knipe, R.J., 2002. Empirical estimation of fault rock properties, *Norwegian Petroleum Society Special Publications,* Vol. **11,** pp. 109–125, Elsevier.

Sridhar, M. & Yovanovich, M.M., 1996. Thermal contact conductance of tool steel and comparison with model, *Int. J. Heat Mass Tran.,* **39,** 831–839.

Sulem, J. & Famin, V., 2009. Thermal decomposition of carbonates in fault zones: Slip-weakening and temperature-limiting effects, *J. Geophys. Res.,* **114**(B3), B03309.

Sulem, J., Vardoulakis, I., Ouffroukh, H. & Perdikatsis, V., 2005. Thermo-poro-mechanical properties of the aigion fault clayey gouge-application to the analysis of shear heating and fluid pressurization, *Soils Found.,* **45**(2), 97–108.

Taboada, A., Chang, K.-J., Radjaï, F. & Bouchette, F., 2005. Rheology, force transmission, and shear instabilities in frictional granular media from biaxial numerical tests using the contact dynamics method, *J. Geophys. Res.,* **110**(B9).

Taboada, A., Estrada, N. & Radjaï, F., 2006. Additive decomposition of shear strength in cohesive granular media from grain-scale interactions, *Phys. Rev. Lett.,* **97**(9), 098302.

Tinti, E., 2005. A kinematic source-time function compatible with earthquake dynamics, *Bull. Seismol. Soc. Am.,* **95**(4), 1211–1223.

Tinti, E., Spudich, P. & Cocco, M., 2005. Earthquake fracture energy inferred from kinematic rupture models on extended faults, *J. Geophys. Res.,* **110,** B12303.

Tinti, E., Scuderi, M.M., Scognamiglio, L., Di Stefano, G., Marone, C. & Collettini, C., 2016. On the evolution of elastic properties during laboratory stick-slip experiments spanning the transition from slow slip to dynamic rupture, *J. Geophys. Res.,* **121**(12), 8569–8594.

Togo, T. & Shimamoto, T., 2012. Energy partition for grain crushing in quartz gouge during subseismic to seismic fault motion: an experimental study, *J. Struct. Geol.,* **38,** 139–155.

Togo, T., Yao, L., Ma, S. & Shimamoto, T., 2016. High-velocity frictional strength of longmenshan fault gouge and its comparison with an estimate of friction from the temperature anomaly in wfsd-1 drill hole, *J. Geophys. Res.,* **121**(7), 5328–5348.

Torabi, A. & Berg, S.S., 2011. Scaling of fault attributes: a review, *Mar. Petrol. Geol.,* **28**(8), 1444–1460.

Vakis, A.I. *et al.*, 2018. Modeling and simulation in tribology across scales: an overview, *Tribol. Int.,* **125,** 169–199.

Vargas, W.L. & McCarthy, J.J., 2001. Heat conduction in granular materials, *AIChE J.,* **47**(5), 1052–1059.

Verberne, B.A., Spiers, C.J., Niemeijer, A.R., De Bresser, J. H.P., De Winter, D. A.M. & Plümper, O., 2014. Frictional properties and microstructure of calcite-rich fault gouges sheared at sub-seismic sliding velocities, *Pure Appl. Geophys.,* **171**(10), 2617–2640.

Violay, M., Nielsen, S., Gibert, B., Spagnuolo, E., Cavallo, A., Azais, P., Vinciguerra, S. & Di Toro, G., 2014. Effect of water on the frictional behavior of cohesive rocks during earthquakes, *Geology,* **42**(1), 27–30.

Vora, H.B. & Morgan, J.K., 2019. Microscale characterization of fracture growth and associated energy in granite and sandstone analogs: Insights using the discrete element method, *J. Geophys. Res.,* **124**(8), 7993–8012.

Wang, Y.F., Dong, J.J. & Cheng, Q.G., 2017. Velocity-dependent frictional weakening of large rock avalanche basal facies: Implications for rock avalanche hypermobility?, *J. Geophys. Res.,* **122**(3), 1648–1676.

Waples, D.W. & Waples, J.S., 2004. A review and evaluation of specific heat capacities of rocks, minerals, and subsurface fluids. Part 1: minerals and nonporous rocks, *Nat. Resour. Res.,* **13**(2), 97–122.

Yovanovitch, M.M., 1967. Thermal contact resistance across elastically deformed spheres, *J. Spacecraft Rockets,* **4,** 119–122.

SUPPORTING INFORMATION

Supplementary data are available at *GJI* online.

Fig. S1. Strength, physical, and geometrical parameters of the shear zone and the granular sample as a function of slip distance or time (x and t) for the reference model ($\sigma_n' = 112.5$ MPa and $V_S = 1$ m s^{-1}) and four values of the flash-heating temperature T_w (runs 2a-d, parametric study II, Table S1). The three phases of mechanical behavior are bounded by vertical color lines and stripes. Dashed curves are exponential approximations of friction and gouge dilatancy; sigmoidal approximation curves for friction and dilatancy in phase 3 are plotted with dots and cross symbols (concave and convex segments, respectively). x_{1-2}: Slip distance at transition between phases 1 and 2; x_{2-3}: Onset of thermal weakening; Ψ_S: Sample dilatancy.

Fig. S2. Spectrograms calculated as a function of slip distance or time (x and t) illustrating the average evolution of damage and temperature (β and T) in the shear zone for the reference model (σ_n'=112.5 MPa and $V_S = 1$ m s^{-1} and four values of the flash-heating temperature T_W (runs 2a-d, parametric study II, Table S1, Fig. S1). The average state of the granular sample at a given slip distance is represented by a vertical profile obtained by calculating average values of parameters within thin horizontal slices. Vertical color lines indicate the onset of thermal weakening (x_{2-3}); dashed curves are logarithmic approximations of contour level $\beta = 0.8$, bounding the gouge zone. The right column shows a microscale view of the shear zone for slip distance x_{2-3}.

Fig. S3. Dilatancy of the sample and the top and bottom cohesive blocks as a function of slip distance or time (x and t) for the reference model ($\sigma_n' = 112.5$ MPa and $V_S = 1$ m s^{-1}) and flash-heating temperature $T_w = 700$ °C (run 2c, parametric study II, Table S1).

Fig. S4. Strength, physical, and geometrical parameters of the shear zone and the granular sample as a function of slip distance (or time) for the reference model ($\sigma_n' = 112.5$ MPa and $V_S = 1$ m s^{-1}) and three values of density for the top wall (runs 3a–c, parametric study III, Table S1). The three phases of mechanical behavior are bounded by vertical color lines and stripes. x_{2-3}: Onset of thermal weakening; Ψ_S: Sample dilatancy.

Fig. S5. Spectrograms calculated as a function of slip distance or time (x and t) illustrating the average evolution of damage and temperature (β and T) in the shear zone for the reference model ($\sigma_n' = 112.5$ MPa and $V_S = 1$ m s^{-1}) and three values of density for the top wall (*cf.* runs 3a–c, parametric study III, Table S1, Fig. S4). The average state of the granular sample at a given slip distance is represented by a vertical profile obtained by calculating average values of parameters within thin horizontal slices. Vertical color lines indicate the onset of thermal weakening (x_{2-3}); dashed curves are logarithmic approximations of contour level $\beta = 0.8$, bounding the gouge zone. The right column shows a microscale view of the shear zone for slip distance x_{2-3}. Particles are colored according to their finite rotation angle (positive anticlockwise).

Fig. S6. Strength, physical, and geometrical parameters of the shear zone and the granular sample as a function of time for the reference model ($\sigma_n' = 112.5$ MPa and $V_S = 1$ m s^{-1}) and three values of the slope of the velocity step (runs 4a–c, parametric study IV, Table S1). Vertical color lines and stripes indicate the onset of thermal weakening. t_{1-2}: Time at transition between phases 1 and 2; t_{2-3}: onset time of thermal weakening.

Fig. S7. Spectrograms calculated as a function of shearing time illustrating the average evolution of damage and temperature (β and T) in the shear zone for the reference model ($\sigma_n' = 112.5$ MPa and $V_S = 1$ m s^{-1}) and three values three values of the slope of the velocity step (*cf.* runs 4a-c, parametric study IV, Table S1, Fig. S6). The average state of the granular sample at a given slip distance is represented by a vertical profile obtained by calculating average values of parameters within thin horizontal slices. t_{1-2}: Time at transition between phases 1 and 2; vertical color lines indicate the onset of thermal weakening (t_{2-3}); dashed curves are logarithmic approximations of contour level $\beta = 0.8$, bounding the gouge zone. The right column shows a microscale view of the shear zone at the strength peak (phase 1). Particles are colored according to the average damage of cohesive bonds.

Table S1. Summary of variables used in runs for parametric studies I–IV. The initial temperature T_0 is equal to 300 °C for all runs.

Please note: Oxford University Press is not responsible for the content or functionality of any supporting materials supplied by the authors. Any queries (other than missing material) should be directed to the corresponding author for the paper.

APPENDIX A: NUMERICAL FRAMEWORK

We use the Contact Dynamics method (CD) proposed by Moreau (Moreau 1988) to solve the dynamic behavior of the granular assembly. Often used in the context of granular material investigation (Estrada *et al.* 2011; Azéma *et al.* 2015), this method has also been used several times in tribological applications (Renouf & Berthier 2011; Champagne *et al.* 2014; Riviere *et al.* 2015).

The CD method is based on an implicit time discretized formulation of the equation of motion written for a collection of particles. Since the number of contacts is higher than the number of particles (dense particle assemblies), the interaction between particles is not considered at the scale of each individual particle but at each contact scale.

To describe the evolution of a collection of particles, the equation of dynamics can be written as:

$$\mathbb{M}\ddot{\mathbf{q}} + \mathbf{F}^{int}(t, \mathbf{q}, \dot{\mathbf{q}}) = \mathbf{F}^{ext}(t, \mathbf{q}, \dot{\mathbf{q}}) + \mathbf{R}, \tag{A1}$$

where $\mathbb{M}$ represents the mass matrix, $\mathbf{F}^{int}(t, \mathbf{q}, \dot{\mathbf{q}})$ are the internal force and the nonlinear inertia terms, $\mathbf{F}^{ext}(t, \mathbf{q}, \dot{\mathbf{q}})$ the external forces, and $\mathbf{R}$ the contact forces. Vector $\mathbf{q}$ represents the vector of generalized degrees of freedom while $\dot{\mathbf{q}}$ and $\ddot{\mathbf{q}}$ denote the generalized velocity and acceleration vectors respectively.

To transfer information from the contact frame (local level) to the body frame (global level), two linear mappings, denoted $\mathbb{H}$ and its transpose $\mathbb{H}^*$, are used.

Thus, the local contact force vector $\mathbf{r}$ and the local relative velocity vector $\mathbf{u}$ can be related to the global body contact force vector $\mathbf{R}$ and the body velocity vector $\dot{\mathbf{q}}$ as:

$$\begin{cases} \mathbf{R} = \mathbb{H}\mathbf{r} \\ \mathbf{u} = \mathbb{H}^*\dot{\mathbf{q}} \end{cases}. \tag{A2}$$

Both mappings depend on local information such as the local frame defined at each contact point and the network connectivity of each contact.

Using the set of eqs (A2) and a θ time integrator scheme (Jean 1999), it is possible to reformulate eq. (A1) in the contact frame. This allows to us write, at each time step, the system (A3) containing the equations of motion:

$$\begin{cases} \mathbb{W}\mathbf{r} - \mathbf{u} & = \mathbf{b} \\ law_\alpha[\mathbf{u}_\alpha, \mathbf{r}_\alpha] & = true, \alpha = 1, n_c \end{cases}, \tag{A3}$$

where the matrix $\mathbb{W}$ is the Delassus operator, containing local information (such as local frames and contact points) allowing it to be used at the particle scale. The vectors $\mathbf{u}$ and $\mathbf{r}$ are respectively the vectors containing the relative velocity and the mean contact impulse for all the contact points of all particles. $\mathbf{b}$ represents the free relative velocity calculated by taking into account the external forces only. The θ-method is used for time discretization and a classical non-linear Gauss-Seidel algorithm is used to solve the system (A3) (Jean 1999). The approach benefits from a parallel version to ensure reasonable CPU times (Renouf *et al.* 2004).

APPENDIX B: HEAT GENERATION AND CONDUCTION IN DISCRETE MEDIA

The temperature of particles in a discrete medium can be tracked considering conductive, radiative or convective effects leading to the thermal evolution eq.(B1):

$$\rho_i c_i V_i \frac{dT_i}{dt} = Q_i^{gen} + Q_i^{cond} + Q_i^{conv} + Q_i^{rad}, \tag{B1}$$

where ρ_i is the mass density, c_i, the specific heat and V_i, the volume of particle i. Q_i^{cond} corresponds to the local conductive heat flux received by the element ij subjected to multiple static interactions. Q_i^{gen} is the local generative heat flux produced when two particles enter in contact dynamically, Q_i^{conv} is the local convective heat flux with a fluid environment and Q_i^{rad} is the local radiative heat flux exchanged. As exposed in the Section 2.3, Q_i^{conv} and Q_i^{rad} are not of the first order when a dense gouge is considered (Richard *et al.* 2008). They are considered as null in the proposed model.

B1 Heat generation

When two particles come into contact, the variation of their kinetic energy can be source of heat generation. This energy, denoted E_{ij}, is written as:

$$E_{ij} = \mathbf{r}_\alpha \mathbf{v}_\alpha, \tag{B2}$$

where $\mathbf{r}_\alpha$ is the local contact force and $\mathbf{v}_\alpha$ the contact relative velocity associated to contact α. This energy is assumed to be split into two equal parts. Thus according to such hypotheses, for the contact α involving particles i and j, the local generated heat flux Q_{ij}^{gen} acting on a particle is written as:

$$Q_{ij}^{gen} = \frac{\psi}{2} E_{ij}. \tag{B3}$$

The parameter ψ is introduced to consider, eventually, only a part of such an energy (Kennedy 1981). Nevertheless, as proposed in (Renouf & Berthier 2011), other forms of energy transformation, such as the convertion into vibrations, phase transformations or the volumetric heat released by plastic strain (Kennedy 1981), are not considered and all the dissipated mechanical energy is converted into thermal energy (i.e. $\psi = 1$). Note that even if the value of ψ

$\neq 1$ modulates the amount of generated heat, the induced variation will be similar for all simulations. Note that even if the value of $\psi \neq 1$ modulates the amount of generated heat, the induced variation will be similar for all simulations. Consequently, quantitative comparisons between runs are pertinent, provided that ψ has a constant value.

B2 Heat transfer

The model for heat transfer between rigid bodies is based on the pioneering work by Yovanovich (Cooper *et al.* 1969; Sridhar & Yovanovich 1996), which was subsequently applied to large discrete element assemblies by Vargas *et al.* (Vargas & McCarthy 2001). The principles of this approach are as follows:

Let α be a contact involving two particles termed i and j. Then the local conductive heat flux can be expressed as:

$$Q_{ij}^{cond} = H(T_i - T_j), \tag{B4}$$

where T_i and T_j are the temperatures of discrete elements i, j and H is the Thermal Contact Conductance (TCC), which contains the thermal behavior related to the micro-structural evolution of the contact. Several authors have proposed accurate representations of H required for a reliable estimation of contact temperatures (Cooper *et al.* 1969; Sridhar & Yovanovich 1996; Laraqi & Bairi 2002). However, their model of asperity contacts between two contacting bodies is static.

In discrete assemblies, H, denoted H^d, derives from Hertz's elastic contact theory (Yovanovitch 1967):

$$H^d = 2k_{th}a. \tag{B5}$$

This parameter is the product of the thermal conductivity k_{th} and the contact area radius a. In a 2-D problem, a contact between two disks is treated as a contact between two cylinders of unit length ($L = 1$). In this case, from eq. (B5), a represents the half-width of the rectangle contact area:

$$a = \sqrt{\frac{4(r_n + \gamma)r^*}{\pi L E^*}}, \tag{B6}$$

where r^* is the effective radius, E^* is Young modulus, γ is the cohesive force, and r_n is the normal component of the contact force.

When DEMs are used to represent an equivalent continuous medium, eq. (B6) cannot be used directly without increasing its thermal resistance. The TCC should be adapted to obtain an equivalent behavior from a thermal point of view. Using an analogy between the contact network and a finite difference method (FDM), a formulation is proposed for the computation of H in a bonded granular media (Riviere *et al.* 2015), noted H^c, defined by:

$$H^c = \frac{\pi k_{th}}{\nu}. \tag{B7}$$

where ν is the number of contacts of the considered particle.

B3 Thermal boundary conditions

The control of the thermal boundary conditions is fundamental in discrete approaches. A lack of boundary conditions can generate adiabatic systems and thus parasitize the evolution of the temperature field. Depending on the system under study, the way in which heat exchange takes place at the boundary must therefore be chosen carefully.

In our study, we use the approach proposed by Renouf & Berthier (2011), in which the boundaries are treated as fictitious walls whose thickness is discretized using a 1D finite difference model. For this purpose, we impose a temperature of 300°C on the external boundary of the walls. The temperature values in the internal boundaries of the walls is given by the top and bottom temperatures of the granular sample. At each time step, this temperature is updated according to the thermal effects within the sample and by solving the heat equation describing the fictitious wall (more details in Renouf & Berthier (2011)). It can be noted, however, that in our simulations the temperature of the upper wall is not affected by the temperature increase around the shear zone. Therefore, these conditions have almost no effect on the behavior of the fault.